



Published in final edited form as:

Cell Rep Phys Sci. 2023 October 18; 4(10): . doi:10.1016/j.xcrp.2023.101584.

Head-to-head comparison of *in vitro* and *in vivo* efficacy of pHLIP-conjugated anti-seed gamma peptide nucleic acids

Karishma Dhuri¹, Tibo Duran¹, Bodhisattwa Chaudhuri^{1,2}, Frank J. Slack³, Ajit Vikram⁴, Peter M. Glazer⁵, Raman Bahal^{1,6,*}

¹Department of Pharmaceutical Sciences, University of Connecticut, Storrs, CT 06269, USA

²Department of Chemical & Biomolecular Engineering, University of Connecticut, Storrs, CT 06269, USA

³HMS Initiative for RNA Medicine, Department of Pathology, BIDMC Cancer Center, Harvard Medical School, 330 Brookline Avenue, Boston, MA 02215, USA

⁴Department of Internal Medicine, Carver College of Medicine, University of Iowa, Iowa City, IA 52242, USA

⁵Department of Therapeutic Radiology, Yale University School of Medicine, New Haven, CT 06520, USA

⁶Lead contact

SUMMARY

Gamma peptide nucleic acids (γ PNAs) have recently garnered attention in diverse therapeutic and diagnostic applications. Serine and diethylene-glycol-containing γ PNAs have been tested for numerous RNA-targeting purposes. Here, we comprehensively evaluated the *in vitro* and *in vivo* efficacy of pH-low insertion peptide (pHLIP)-conjugated serine and diethylene-based γ PNAs. pHLIP targets only the acidic tumor microenvironment and not the normal cells. We synthesized and parallelly tested pHLIP-serine γ PNAs and pHLIP-diethylene glycol γ PNAs that target the seed region of microRNA-155, a microRNA that is upregulated in various cancers. We performed an all-atom molecular dynamics simulation-based computational study to elucidate the interaction of pHLIP- γ PNA constructs with the lipid bilayer. We also determined the biodistribution and efficacy of the pHLIP constructs in the U2932-derived xenograft model. Overall, we established that the pHLIP-serine γ PNAs show superior results *in vivo* compared with the pHLIP-diethylene glycol-based γ PNA.

This is an open access article under the CC BY-NC-ND license (<http://creativecommons.org/licenses/by-nc-nd/4.0/>).

*Correspondence: raman.bahal@uconn.edu.

AUTHOR CONTRIBUTIONS

Conceptualization, R.B. and K.D.; methodology, R.B. and K.D.; investigation, K.D.; MD simulation study, T.D.; writing – original draft, R.B. and K.D.; writing – review and editing, R.B., K.D., T.D., F.J.S., B.C., A.V., and P.M.G.; funding acquisition, R.B. and F.J.S.; supervision, R.B.

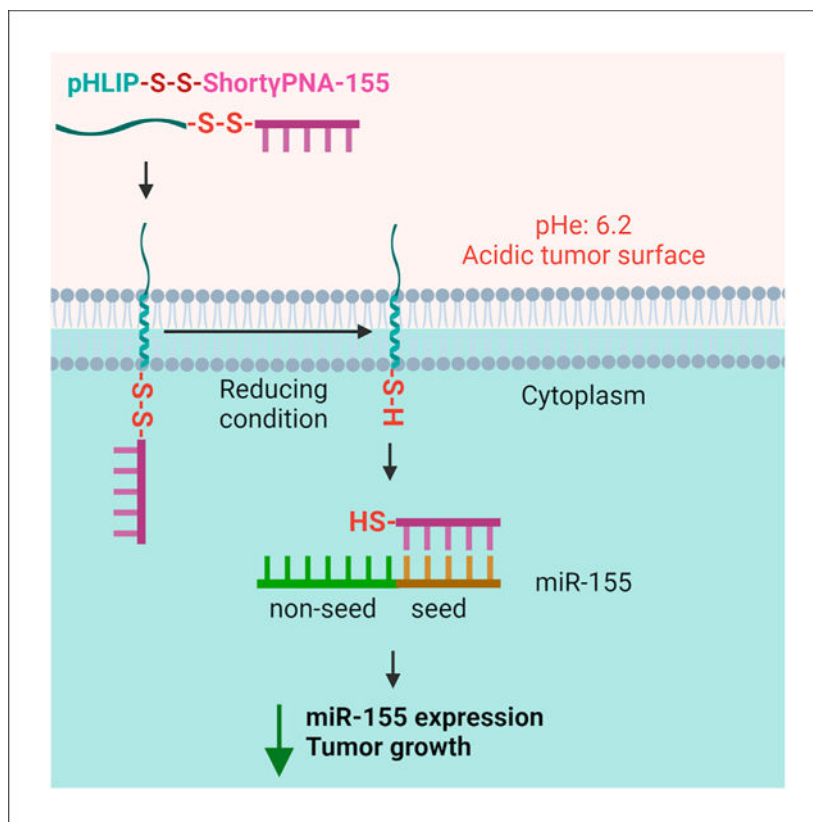
SUPPLEMENTAL INFORMATION

Supplemental information can be found online at <https://doi.org/10.1016/j.xcrp.2023.101584>.

DECLARATION OF INTERESTS

The authors declare no competing interests.

Graphical Abstract



Dhuri et al. compared the biophysical, cell culture, and *in vivo* efficacy of pHILIP-diethylene glycol γ PNA and pHILIP-serine γ PNA conjugates. *In vivo* inhibition of microRNA-155 by pHILIP- γ PNA results in the upregulation of multiple microRNA-155 target tumor suppressor genes and reduced tumor growth.

INTRODUCTION

MicroRNAs (miRNAs) are small noncoding RNAs (18–20 nt long) that bind to the 3' untranslated region of protein-coding genes and control gene expression.¹ It has been well established that miRNAs play a crucial role in key physiological processes, such as growth, proliferation, apoptosis, and survival.² Various strategies have been attempted to inhibit dysregulated miRNA, including small-molecule-based inhibitors, miRNA sponges, and anti-miR designs containing phosphorothioate, locked nucleic acid, and 2' O modification chemistry.^{3–14} Various synthetic nucleic acid chemistries have been used to inhibit disease-associated miRNAs.^{15–18} In particular, peptide nucleic acids (PNAs) have gained much interest because of their miRNA inhibitory activity.¹⁹

PNAs are synthetic analogs of DNA or RNA in which the phosphodiester backbone is replaced by *N*-(2-aminoethyl) glycine units.²⁰ PNAs possess various attractive properties, such as resistance to enzymatic degradation, and have superior binding affinity to complementary DNA and RNA via Watson-Crick base pairing.²¹ Various chemical

modifications have been performed on the PNA to increase its solubility and binding affinity. Notably, modification of the gamma position of the PNA backbone has been shown to improve its therapeutic properties. It has been shown that installing a chiral center at the gamma position pre-organizes the PNA in a right-handed helical conformation, which further enhances the binding affinity to the complementary nucleic acids via Watson-Crick base pairing.²² Hence various gamma-modified PNAs, in particular, serine gamma PNAs (γ PNAs; $S\gamma$ PNAs) and diethylene glycol (mPEG) γ PNAs ($M\gamma$ PNAs), have been tested. $S\gamma$ PNAs and $M\gamma$ PNAs contain the hydroxy group or mPEG group as a side chain at the gamma position of the backbone, further enhancing their solubility and binding affinity compared with the regular PNA.²³

Like other nucleic acid analogs, delivery remains a challenge for γ PNAs in improving their potency. We have previously established that pH-low insertion peptide (pHLIP) selectively targets the acidic tumor microenvironment, not the normal bystander cells after systemic delivery.²⁴ The aspartic acid and glutamic acid residues of the pHLIP get protonated in the acidic tumor microenvironment followed by increases in hydrophobicity of the pHLIP. This results in pHLIP folding to form alpha helix from the N to C terminus that partitions across the bilayer as the transmembrane helix.^{25,26} Because cargo is conjugated to the C terminus of pHLIP, under reducing conditions in the cytoplasm, cargo (PNA and γ PNA in this study) is released and binds to the intended target site.²⁷⁻²⁹ We successfully demonstrated that pHLIP could deliver full-length PNAs and exert its miRNA-inhibitory activity.³⁰ Further, to advance the PNA-based anti-miR technology, we also established that poly-lactic-co-glycolic acid-based nanoparticles encapsulated by short anti-seed regular PNAs conjugated with the arginine (Arg) amino acids could target miR-155 effectively.³¹ Similarly, other studies indicated that dendrimer and liposome-based strategies could also be implied to deliver anti-miR PNAs.³² Although nanoparticles and liposomes have shown success to some extent, clearance by the reticuloendothelial system and endosome entrapment are the barriers the nanoparticle system must overcome to be efficacious.^{33,34} The delivery of nanoparticles to the tumor depends on the enhanced permeability and retention (EPR) effect and tumor vasculature.³⁵ Therefore, alternative methods to deliver PNAs are needed to circumvent these issues and provide tumor-targeted delivery.³⁶ We noted that pHLIP-based delivery platforms offer an advantage over solid nanoparticle-based delivery strategies because they do not rely on the EPR effect and do not undergo endosomal entrapment because of a lack of uptake through endocytic pathways.²⁶ However, prior work established that pHLIP could not deliver charged molecules across the membrane. Hence, testing the non-cationic chemically modified gamma anti-seed PNA with an optimal binding affinity that inhibits the miRNA is imperative.

In different formulations and pHLIP conjugates, PNA and γ PNA have been tested *in vivo* for toxicity analysis. It is well established that PNA- and γ PNA-based therapeutic modalities do not exert any adverse cell-, organ-, and immune-based toxicity. Prior studies demonstrated that oligonucleotides with negative-charge backbone or CG dinucleotide repeat exhibit immune and non-specific binding-based toxicity.³⁶⁻⁴² In contrast, PNAs containing neutral backbone do not cause activation of an immune response.

Here, we comprehensively tested the next-generation S γ PNAs and miniPEG γ PNAs in conjunction with the pHLIP. We also tested *in vitro* and *in vivo* efficacy in the U2932 lymphoma cell line and in the U2932 cell-line-derived xenograft mouse model. The results presented in this study demonstrate the feasibility of an approach where short γ PNA can be delivered via the pHLIP delivery system. In this study, we made a head-to-head comparison of pHLIP-conjugated S γ PNA- and M γ PNA-based technologies. Overall, this technology can be utilized to deliver antisense oligomer for diverse therapeutic applications.

RESULTS

Anti-seed γ PNA designs and biophysical analysis

We tested the miRNA-inhibitory activity of three different PNA chemistries: regular PNA (PNA 1), mPEG-containing γ PNA (M γ PNA 2), and S γ PNA (S γ PNA 3) (Figure 1A). We designed and synthesized short anti-seed (8-nt) γ PNAs targeting the seed region of miR-155 (Figure 1B). The N terminus corresponds to 5' end and C terminus corresponds to the 3' end of the PNA. A cysteine (C) amino acid was incorporated at the 3' termini of the PNA sequences to facilitate conjugation with pHLIP. We synthesized control scrambled γ PNA (Scr-S γ PNA 4). We attached a 5-carboxytetramethylrhodamine (Tamra) fluorophore at the 5' PNA to probe cellular uptake and biodistribution in xenograft mice (PNA T5, M γ PNA T6, S γ PNA T7; Figure 1). We synthesized full-length regular PNA (PNA 8) to compare its activity relative to short S γ PNA (S γ PNA 3). All the PNAs were synthesized using solid-phase synthesis followed by reverse-phase high-performance liquid chromatography (RP-HPLC) purification.

The binding affinity of the PNA/ γ PNA to the miR-155 target was evaluated using thermal denaturation (melting) analysis (Figure 1C). We noted that M γ PNA 2 and S γ PNA 3 showed higher thermal melting (50.6°C and 52.6°C, respectively) compared with the regular PNA 1 (40.7°C). These results were expected as gamma-modified PNAs pre-organize to a right-handed helical structure resulting in the enhanced binding affinity to the target. We noted a slight increase (2.0°C) in the thermal melting of S γ PNA 3 compared with M γ PNA 2.

Next, we conjugated the PNA/ γ PNAs to pHLIP by disulfide exchange reaction. The pHLIP-PNA/ γ PNAs conjugates were purified by RP-HPLC (Figure S1). We also evaluated the binding affinity of pHLIP-PNA and pHLIP- γ PNA constructs to the target miR-155 by gel shift assay (Figure 1D). The samples were incubated at physiological salt conditions and temperature for 1 h. The reducing agent tris 2-carboxyethyl phosphine (TCEP) was used to simulate the disulfide bond cleavage. We did not notice a retarded band for PNA 1 (Figure 1D, lanes 2–4). M γ PNA 2 and S γ PNA 3 showed considerable binding with the miR-155 target, as observed by retarded bands (Figure 1D, lanes 6 and 10). The upper band corresponds to the complex of M γ PNA 2 dimer with miR-155 (Figure 1D, lane 6) and the complex of S γ PNA 3 dimer with miR-155 (Figure 1D, lane 10). The pHLIP-M γ PNA 2 and pHLIP-S γ PNA 3 also showed binding with the target miR-155 as indicated by retarded bands (Figure 1D, lanes 7 and 11). The M γ PNA 2 and S γ PNA 3 complexes exhibited significant binding with the miR-155 target in the presence of TCEP (Figure 1D, lanes 8 and 12). We also quantified the binding affinity by measuring the intensity of the unbound fraction by ImageJ software (Figure S2).

Molecular dynamics simulation of pHLIP-PNA/ γ PNA interaction with membrane bilayer

We compared the insertion depth of pHLIP-PNA 1, pHLIP-M γ PNA 2, and pHLIP-S γ PNA 3 in the 1,2-dipalmitoylphosphatidylglycerol (DPPG) membrane bilayer (Figure 2A). The pHLIP-PNA 1, pHLIP-M γ PNA 2, and pHLIP-S γ PNA 3 are horizontally positioned above the membrane bilayer at the initial start point of 0 ns. The pHLIP-PNA 1, pHLIP-M γ PNA 2, and pHLIP-S γ PNA 3 insert in the upper bilayer leaflet at 750 ns. The pHLIP-PNA 1 and pHLIP-M γ PNA 2 partially insert in the upper leaflet of bilayer at 1,000 ns. The pHLIP-S γ PNA 3 traverses the upper leaflet of the bilayer at 1,000 ns. We observed distinct transitions in pHLIP-PNA 1, pHLIP-M γ PNA 2, and pHLIP-S γ PNA 3 conformations at 750 and 1,000 ns (Figure S3).

We next evaluated molecular interaction energy of pHLIP-PNA 1, pHLIP-M γ PNA 2, and pHLIP-S γ PNA 3 with DPPG membrane bilayer using van der Waals (vdW) energy versus time plot (Figure 2B). The pHLIP-PNA 1 (black) and pHLIP-S γ PNA 3 (pink) showed a rapid energy gain (or significant reduction) of $-1,300 \text{ kJ mol}^{-1}$ on first contact with the upper leaflet at 200 ns, whereas pHLIP-M γ PNA 2 (blue) showed an energy gain of -650 kJ mol^{-1} at 200 ns. The pHLIP-PNA 1 and pHLIP-M γ PNA 2 showed a modest gain of $-1,500 \text{ kJ mol}^{-1}$ between 200 and 1,000 ns. The pHLIP-S γ PNA 3 exhibited an energy gain of $-1,700 \text{ kJ mol}^{-1}$ between 200 and 1,000 ns. The more negative interaction energy value indicates the increased attraction between pHLIP-S γ PNA 3 and the membrane bilayer.

The define secondary structure of proteins (DSSP) program was employed to study the secondary structure transitions based on hydrogen bonds and geometric patterns from 0 to 1,000 ns for pHLIP-PNA 1, pHLIP-M γ PNA 2, and pHLIP-S γ PNA 3 (Figure 2C). The N terminus (residue no. 1) for pHLIP-PNA 1 (Figure 2C, top, blue) and pHLIP-S γ PNA (Figure 2C, bottom, blue) exhibited helical conformations from 0 to 1,000 ns. The pHLIP-M γ PNA 2 showed helical conformations up to 600 ns (Figure 2C, center, blue). The C terminus (residue no. 37, where pHLIP is conjugated to PNA/ γ PNAs) of pHLIP-PNA 1, pHLIP-M γ PNA 2, and pHLIP-S γ PNA 3 exhibited coils, bends, and turns (shown in white, green, and yellow, respectively). The pHLIP-PNA 1 (Figure 2C, top, residue no. 10–37) transitioned from a helical structure to coil, bend, and turn orientations between 400 and 1,000 ns. The middle portion of pHLIP-M γ PNA 2 (Figure 2C, center, residue no. 10–28) and pHLIP-S γ PNA 3 (Figure 2C, bottom, residue no. 10–16 and 23–28) retained the helical structures. We observed very few alpha-helical structures for pHLIP-PNA (Figure 2C, top, residue no. 3–10) and alpha-helical, 5-helical (maroon) structures for pHLIP-M γ PNA 2 (Figure 2C, center, residue no. 17–28) at 1,000 ns. The N terminus (Figure 2C, bottom, residue no. 4–16 and 24–28) of pHLIP-S γ PNA 3 shows alpha helix, 5-helix, and 3-helix (gray) at 1,000 ns. The flexibility of pHLIP-PNA/pHLIP- γ PNA was evaluated in detail by performing the analysis of the root-mean-square fluctuations (RMSFs) (Figure S4). The degree of flexibility of each residue in pHLIP-PNA and pHLIP- γ PNA conjugates with respect to time-averaged coordinates was calculated at 300 K to determine the influence of PNA and γ PNA on the flexibility pHLIP structure. The pHLIP structure was highly flexible when conjugated to PNA 1 (black) and M γ PNA 2 (blue), as indicated by the RMSF values ranging from 0.217 to 0.622 nm (a difference of 0.405 nm) and 0.656 to 0.160 nm (a difference of 0.496 nm), respectively. The flexibility of the pHLIP structure was

reduced, and it exhibited fluctuations within only a narrow range of 0.285–0.554 nm (a difference of 0.269 nm) when conjugated to S γ PNA 3 (pink). The C terminus (residue no. 33–35) of pHLIP-PNA 1 and pHLIP-M γ PNA 2 had higher flexibility than pHLIP-S γ PNA 3. These results suggest higher stability (because of lower fluctuations) of pHLIP-S γ PNA 3 in maintaining the helical conformation that aids in the membrane insertion process.

The mass density profiles along the bilayer normal (z coordinate) for phosphate head and glycerol esters were calculated (Figures 2D, 2E, and S5). The bilayer thickness calculated as the distance between the peaks of the phosphate head groups was approximately 4 nm for pHLIP-PNA 1, pHLIP-M γ PNA 2, and pHLIP-S γ PNA 3. The mass density of the upper and lower leaflets exhibited different patterns, with pHLIP-S γ PNA 3 showing a higher degree of asymmetry (Figure 2D, bottom, density difference between two peaks is 156 kg m⁻³) than pHLIP-M γ PNA 2 (Figure 2D, center, slightly asymmetric with a density difference of 99 kg m⁻³) and pHLIP-PNA (Figure 2D, top, density difference of 24 kg m⁻³). A similar asymmetry was observed for glycerol ester groups, with the upper monolayer having a much lower density relative to the lower monolayer for pHLIP-S γ PNA 3 insertion (Figure 2E, bottom, density difference 160 kg m⁻³) than for pHLIP-M γ PNA 2 insertion (Figure 2E, center, difference 111 kg m⁻³) and pHLIP-PNA insertion (Figure 2E, top, density difference of 8 kg m⁻³). A higher degree of asymmetry in the mass density of phosphate head groups and glycerol esters for pHLIP-S γ PNA 3 signifies greater membrane insertion.

Cellular uptake in U2932 lymphoma cells

We evaluated the cellular uptake of pHLIP-PNA-Tamra and pHLIP- γ PNA-Tamra in U2932 lymphoma cells. This experiment was conducted in acidic pH (6.4) media to mimic the acidic tumor microenvironment. We performed cellular uptake of pHLIP-PNA T5, pHLIP-M γ PNA T6, and pHLIP-S γ PNA T7 in U2932 cells at 500 nM dose after 4-h treatment duration. Our confocal results reveal that pHLIP-S γ PNA T7 showed more cellular uptake than pHLIP-PNA T5 and pHLIP-M γ PNA T6 (Figure 3A). Based on the flow cytometry results, we also observed higher uptake of pHLIP- γ SPNA T7 compared with other controls (Figure 3B). Overall, pHLIP-S γ PNA T7 showed ~3.5-fold higher uptake in U2932 cells as compared with pHLIP-PNA T5 and pHLIP-M γ PNA T6 (Figure 3C). Because the pHLIP-serine gamma-modified PNA showed a higher binding affinity to miR-155 target (Figures 1B and 1C) and higher cellular uptake, we designed a scrambled S γ PNA 4 sequence (pHLIP-Scr-S γ PNA 4) for further study.

Evaluation of miR-155 and downstream target levels in U2932 cells

We assessed the extent of miR-155 inhibition in U2932 lymphoma cells after treatment with pHLIP-PNA or pHLIP- γ PNA. We observed a 20%, 30%, and 50% decrease in miR-155 levels after treatment with a 500 nM dose of pHLIP-PNA 1, pHLIP-M γ PNA 2, and pHLIP-S γ PNA 3, respectively, for 24 h (Figure 4A). The full-length PNA 8 showed a 90% decrease in miR-155 levels (Figure S6). We also evaluated the gene expression of miR-155 downstream target genes (Figure 4B). The *CSF1R* levels increased by ~33% with pHLIP-PNA 1 and pHLIP-M γ PNA 2 and by ~83% in the pHLIP-S γ PNA 3-treated group. Inhibiting miR-155 increases the expression of tumor suppressor genes such as *CASPASE3* and *TGP53* that are directly involved in apoptosis.⁴³ The *CASPASE3* levels increased by

20% with pHLIP-PNA 1 and in pHLIP-M γ PNA 2 and by 40% in the pHLIP-S γ PNA 3-treated group. The pHLIP-M γ PNA 2- and pHLIP-S γ PNA 3-treated mice showed an increase in *TGP53* levels by 10% and 30%, respectively. The silencing of miR-155 inhibits tumor cell-cycle progression and induces programmed cell death by upregulating the tumor suppressor gene *FOXO3*.⁴⁴ The pHLIP-PNA 1-, pHLIP-M γ PNA 2-, and pHLIP-S γ PNA 3-treated groups showed an increase in *FOXO3* levels by 10%, 60%, and 60%, respectively. The tumor suppressor gene *BACH1* negatively regulates tumor cell proliferation, apoptosis, and the hypoxia response.⁴⁵ Inhibiting miR-155 increased *BACH1* levels by 20% in the pHLIP-M γ PNA 2- and pHLIP-S γ PNA 3-treated group. Thus, inhibiting miR-155 using pHLIP- γ PNA results in the de-repression of multiple miR-155 target tumor suppressor genes.

Treatment efficacy in U2932 cells

We determined the extent of cell apoptosis using an Annexin V assay and observed a 40% increase in apoptotic cells upon treatment with pHLIP-PNA 1. We also noted a 60% increase in apoptotic cells upon treatment with pHLIP-M γ PNA 2 and pHLIP-S γ PNA 3 (Figure 5A). We next quantified the anti-apoptotic Mcl-1 protein levels by western blot analysis. The pHLIP-PNA 1 showed a 70% decrease in Mcl-1 levels, whereas the pHLIP-S γ PNA 3 showed an 80% decrease in Mcl-1 levels compared with the PBS-treated group (Figure 5B). The PBS- and pHLIP-Scr-S γ PNA 4-treated mice showed similar Mcl-1 levels as expected (Figure S7). We evaluated the efficacy of pHLIP-PNA 1, pHLIP-M γ PNA 2, and pHLIP-S γ PNA 3 in U2932 cells at 500 nM dose by MTS assay (Figure S8). We used pHLIP-Scr-S γ PNA 4 as a sequence scrambled control. The pHLIP-PNA 1 showed an ~10% decrease in U2932 cell viability, whereas pHLIP-M γ PNA 2 and pHLIP-S γ PNA 3 showed ~25% decrease in cell viability (Figure S8).

Biodistribution of pHLIP- γ PNA-Tamra conjugates in U2932 xenograft mice

We performed a biodistribution study to evaluate the tumor targeting of pHLIP- γ PNA conjugates. U2932 xenograft mice were dosed (3 mg kg⁻¹) with pHLIP-PNA T5, pHLIP-M γ PNA T6, and pHLIP-S γ PNA T7 conjugates by systemic delivery via retro-orbital route. Further, we evaluated the fluorescence in mice in the indicated organs and the tumor mass by *in vivo* imaging system (IVIS) imaging 24 h post-injection (Figure 6A). As expected, we noted predominant biodistribution in the tumor for pHLIP-PNA T5, pHLIP-M γ PNA T6, and pHLIP-S γ PNA T7 conjugates (Figure 6A). We noted optimal retention of Tamra in the pHLIP-S γ PNA T7-treated mice followed by M γ PNA T6- and pHLIP-PNA T5-treated groups. As expected, pHLIP showed biodistribution in the kidneys as a result of the acidic environment. We next quantified the fluorescence intensity of the pHLIP-PNA-tamra or pHLIP- γ PNA-tamra in the tumor sections. We found the pHLIP-S γ PNA T7 showed a higher tumor accumulation as compared with pHLIP-PNA T5 and pHLIP-M γ PNA T6 (Figure 6B). We also observed significantly less accumulation of pHLIP-S γ PNA T7 in the kidney compared with pHLIP-PNA T5 and pHLIP-M γ PNA T6 (Figure 6B). Next, we confirmed the uptake of PNA-tamra in the mouse tumor cryosections, confirming its uptake in the tumor cells (Figure 6C).

In vivo efficacy in U2932 xenograft mice

Further, we studied the efficacy of pHLIP- γ PNA conjugates in the U2932-derived xenograft mice. We generated the U2932 cell-line-derived xenograft model based on an established protocol.⁴⁶ We performed multiple dosing (3 mg kg⁻¹) by systemic delivery in the U2932-derived xenograft mice once tumors reached a volume 100–200 mm³ (Figure 7A). Mice were sacrificed once the tumors reached 2 cm³. We noted an increase in survival with the pHLIP-M γ PNA 2- and pHLIP-S γ PNA 3-treated mice compared with pHLIP-PNA-1-treated mice (Figure 7A). We also tested the scrambled control and noted that the survival rate of the PBS and pHLIP-Scr-S γ PNA-4 are similar (Figure S9).

Further, to test for miR-155 engagement, we evaluated the miR-155 levels in the excised tumors. First, we isolated the U2932 tumor cells from the mouse cells by magnetic-bead-based separation. In gene expression analysis, we observed an ~20% decrease in miR-155 levels in pHLIP-PNA 1-treated mice and an ~60% decrease in miR-155 levels in the pHLIP-M γ PNA 2-treated groups. The pHLIP-S γ PNA 3 mice showed an ~65% decrease in miR-155 levels (Figure 7B). Further, we determined the miR-155-regulated tumor suppressor gene expression levels in the tumor samples. We observed an increase in *PICALM*, *BACH1*, *CASPASE 3*, and *CUX1* gene expression levels in pHLIP-M γ PNA 2- and pHLIP-S γ PNA 3-treated mice (Figure 7C). The *PICALM* levels were increased by 40% and 50% for the pHLIP-M γ PNA 2- and pHLIP-S γ PNA 3-treated mice, respectively. The pHLIP-M γ PNA 2- and pHLIP-S γ PNA 3-treated mice showed a 60% increase in *BACH1* levels as compared with pHLIP-Scr-S γ PNA 4-treated mice. We also observed a 45% and 60% increase in *CASPASE3* levels for the pHLIP-M γ PNA 2 and pHLIP-S γ PNA 3 treatment group as compared with the scrambled control. *CUX1* levels increased by 50% and 60% for the pHLIP-M γ PNA 2- and pHLIP-S γ PNA 3-treated mice, respectively. We observed an increase in the *JARID2* by 30% in pHLIP-M γ PNA 2-treated mice, whereas *SHIP1* levels were increased by 40% in pHLIP-S γ PNA 3-treated mice as compared with the pHLIP-Scr-S γ PNA 4-treated mice. The miR-155 and downstream gene expression profiles of PBS and pHLIP-Scr-S γ PNA 4 are similar (Figures S10 and S11).

Further, we determined that the levels of anti-apoptotic protein *Mcl-1*, which is a target for miR-155,⁴⁷ was decreased by 23% in the pHLIP-S γ PNA 3-treated group (Figure 7D). We also confirmed that the pHLIP-S γ PNA 3-treated mice showed a 30% reduction in *Mcl-1* protein levels (Figure 7E).

We next evaluated the Ki-67 levels in the tumor samples by immunohistochemical (IHC) staining. We found that pHLIP-S γ PNA 3-treated mice showed less Ki-67 staining than pHLIP-PNA 1- and pHLIP-M γ PNA 2-treated mice (Figures S12A and S12B).

We also evaluated the H&E sections of the heart, kidney, liver, lung, and spleen of pHLIP-Scr-S γ PNA 4-, pHLIP-PNA 1-, pHLIP-M γ PNA 2-, and pHLIP-S γ PNA 3-treated groups in a blinded manner to ensure its safety (Figure S13). Further, we confirmed the safety of pHLIP- γ PNA conjugates by evaluating a metabolic panel of the liver (alkaline phosphatase, aspartate aminotransaminase, lactate dehydrogenase) and kidney-associated enzymes (blood urea nitrogen, creatinine) in the pHLIP- γ PNA conjugate-treated groups (Table S1). Similarly, a complete blood count profile further confirmed the lack of toxicity

of the pHLIP- γ PNA conjugates (Table S2). We evaluated the safety of the pHLIP-PNA conjugates on human embryonic kidney (HEK293) cells by MTS assay. As expected, the HEK293 cells showed no signs of toxicity when treated with pHLIP-PNA conjugates at a 500 nM dose for 24-h treatment duration (Figure S14). Overall, all the above results strongly point to the safety of pHLIP-PNA and pHLIP- γ PNA conjugates.

DISCUSSION

γ PNA-based antisense inhibitors have shown potential in numerous applications.^{48,49} Depending on the functional groups at the gamma position, various generations of gamma-modified PNAs have been evaluated. Still, the targeted delivery of γ PNA-based inhibitors has been an unresolved area. In addition, the physicochemical and biological properties of γ PNAs have been studied to some extent; however, their properties in conjunction with the specific delivery platforms have not been evaluated. In this study, we performed a head-on comparison of mPEG- and serine-based γ PNAs in conjunction with the pHLIP-based delivery system. We chose the pHLIP-delivery system because it has shown potential in delivering diverse types of cargo in tumor acidic conditions.⁵⁰ In addition, recently, pHLIP has shown prospects in delivering small-molecule-based inhibitors and has been studied in clinical trials.⁵¹

Both mPEG- and serine-based γ PNAs possess superior binding and solubility features compared with regular PNAs. mPEG-based γ PNAs are effective in anti-miR, antisense, and gene-editing-based applications in conjunction with the PLGA nanoparticle-based delivery platforms.⁵² In our prior work, we established that serine-modified γ PNAs have enhanced anti-miR activity compared with the regular PNAs.⁴⁶ To our knowledge, this is the first study where we performed the parallel comparison of the pHLIP-conjugated M γ PNA and S γ PNA. We tested the anti-seed design of both γ PNAs because multiple studies indicated that the anti-seed miRNA inhibitor can target potential miRNA biomarkers and has superior features in terms of ease of synthesis and more druggable properties. It has been established that the chemically modified γ PNAs can exert ample activity without exerting any sequence-specific off-targets.²⁸

In this study, we synthesized short anti-seed γ PNA-based anti-miR-155 oligomers and its pHLIP conjugates. Initial thermal denaturation studies indicated a higher thermal binding of M γ PNA 2 and S γ PNA 3 than the regular PNA 1. These results were anticipated because γ PNAs have a preorganized helical conformation that increases their binding affinity with miR-155. Further, we established the binding of pHLIP-M γ PNA 2 and pHLIP-S γ PNA 3 in reducing and non-reducing conditions with miR-155 by gel shift assays. Also, we confirmed their superior binding affinity compared with the regular PNAs. Further, we evaluated their cellular uptake by confocal microscopy and flow cytometry analysis and noted that pHLIP-S γ PNA conjugates demonstrate slightly superior uptake, followed by the M γ PNA-based conjugates. One plausible mechanism could be increased internalization because of more stable alpha-helical formation. Further, cell-culture-based uptake studies in the presence of endocytic inhibitors are required to decode the actual uptake mechanism. The increased uptake can be related to the conformation of the pHLIP- γ PNA conjugates. Circular dichroism studies are insufficient to determine the conformation because of overlapping

maxima and minima of helical γ PNA and pHLIP. Advanced studies using small-angle X-ray scattering (SAXS), small-angle neutron scattering (SANS), and atomic force microscopy (AFM) can be performed to determine the conformation of pHLIP- γ PNA conjugates.^{53,54}

Further, we also attempted to understand the mechanisms of pHLIP- γ PNA conjugates by using computational tools. The calculations of vdW energy indicate that the different forms of partial insertion can be achieved thermodynamically at a temperature of 300 K. At an acidic pH, pHLIP conjugates become more hydrophobic, which makes it more energetically favorable to insert into the 1-palmitoyl-2-oleoyl-phosphatidylcholine (POPC) bilayer. The initial rapid increase in energy and strong interaction observed during the first reduction (Figure 2B) may be attributed to the increased hydrophobicity of pHLIP resulting from the protonation of the transmembrane residue Asp and the C-terminal residues Asp/Glu (glutamate). This increase in hydrophobicity was also suggested by a previous study.⁵⁵ Furthermore, the evaluation of the center-of-mass (COM) distance indicates that pHLIP-S γ PNA 3 is inserted deeper into the bilayer (Figure 2A), and the stronger interaction energy further confirms that S γ PNA facilitates entry into the bilayer. This is because the initial helical structure of pHLIP was more pronounced and was better preserved in pHLIP-S γ PNA 3 than in any of the other conjugates depicted in Figure 2C. This is also evident in the analysis of the RMSFs (Figure S4), which shows that the residues in pHLIP-S γ PNA3 are more stabilized, which could also be caused by the more stable structure of pHLIP-S γ PNA 3.⁵⁶ Furthermore, the helical structures in both pHLIP-M γ PNA 2 and pHLIP-PNA 1 are lost by 68% and 79%, respectively, of their initial helical structures at 1,000 ns, whereas there is a 50% loss for pHLIP-S γ PNA 3, which indicates the stability of the secondary structure of pHLIP was maintained well by connecting with the S γ PNA fragment. The greater stability of the conjugate, as indicated by the RMSF and DSSP analyses, could improve the interaction between the conjugate and the bilayer, ultimately leading to an increased uptake by the cells.⁵⁷ Recent studies have indicated that the insertion of pHLIP into POPC bilayers causes minimal disruption and does not induce membrane leakage.^{29,58,59} However, when assessing the pHLIP conjugates upon insertion, the difference in mass density of the upper leaflet suggests that the membrane insertion of pHLIP conjugates perturbs the structure of the POPC bilayer to some extent. Nevertheless, what is particularly noteworthy is that the insertion of pHLIP-S γ PNA 3 had a greater impact on the mass density of the lipid phosphate head and glycerol ester groups because of its deeper insertion and stronger interaction with the bilayer, which verified the previous observations and analysis.

Our cell culture studies indicated that pHLIP-S γ PNA 3 showed slightly higher miR-155 gene knockdown than pHLIP-M γ PNA 2. Further, we confirmed better upregulation of tumor suppressor downstream target genes for the pHLIP-S γ PNA 3-treated U2932 cells, followed by pHLIP-M γ PNA 2. These results could be attributed as a result of the higher uptake of pHLIP- γ PNA conjugates. We also corroborated these results with the cell viability analysis and noted an optimal decrease in the cell viability with the pHLIP- γ PNA conjugates. Prior studies centered on RNA sequencing (RNA-seq) studies indicated that PNA can effectively target miR-155, affect the tumor biology, and cause a decrease in the tumor growth.³⁰

pHLIP has made strides in delivering cytotoxic agents, fluorophores, regular PNAs, and cyclic peptides to the acidic tumor microenvironment.⁶⁰ During our biodistribution studies, we noted optimal biodistribution of pHLIP-S γ PNA conjugates followed by pHLIP-M γ PNA. In the prior studies, it was well established that pHLIP constructs also accumulate in the kidneys. Interestingly, the pHLIP-S γ PNA conjugate-treated mice showed significantly lower kidney retention and higher tumor accumulation at 24 h post-injection compared with the pHLIP-PNA T5- and pHLIP-M γ PNA T6-treated mice. Our computational studies indicated that pHLIP-S γ PNA has superior transmembrane insertion compared with the miniPEG-gamma-based constructs, and this may support increased tumor accumulation compared with clearance in the kidneys. Still, the mechanism by which serine-modified γ PNA has better retention in the tumor compared with the diethylene-glycol-based γ PNAs needs to be investigated.

Further, we also confirmed uptake in the tumor cryosections. During *in vivo* efficacy studies, our results indicated that pHLIP-S γ PNA has superior miR-155 inhibitory activity and better survival than the pHLIP-M γ PNA.

Although a detailed mechanistic understanding of cellular translocation of a diverse class of γ PNAs needs to be evaluated, our results show the benefits of S γ PNA over the M γ PNA. Although M γ PNAs have been extensively used in the past for numerous applications, M γ PNAs are still not commercially available. Another major challenge associated with diethylene-based γ PNAs is racemization during the monomer synthesis. The reaction of mPEG with the hydroxy group in the basic conditions can result in potential racemization, which can decrease its efficacy because of the presence of both D and L conformations. In contrast, S γ PNA monomers do not require the additional steps that could cause the racemization.²³ Overall, we demonstrated the feasibility of a S γ PNA-based approach that can be used for various applications, including antisense and gene-targeting-based strategies.

EXPERIMENTAL PROCEDURES

Resource availability

Lead contact—Further information and requests for resources should be directed to the lead contact, Raman Bahal (raman.bahal@uconn.edu).

Materials availability—This study did not generate new unique reagents.

Data and code availability—Data reported in this paper will be shared by the lead contact upon request. This study did not report original code.

PNA synthesis and PNA-pHLIP conjugation: Boc-protected monomers required for regular PNA, miniPEG PNA, and serine PNA synthesis were purchased from ASM Research Chemicals (Hannover, Germany). The monomers were vacuum dried for a week before starting the synthesis. The coupling solution was made fresh for the synthesis. Around 100 mg cysteine-loaded resin was taken in reaction vessel and soaked in dichloromethane (DCM) for around 5 h. The DCM was drained off, and the resin was deprotected using trifluoroacetic acid (TFA):m-cresol (95:5) solution for 5 min (three times).

The resin was washed with DCM and N,N-dimethylformamide (DMF). The monomer was dissolved in coupling solution composed of 0.52 mol/L di-isopropylethylamine and 0.39 mol/L O-benzotriazole-N,N,N',N'-tetramethyl-uronium-hexafluoro-phosphate and 0.2 mol/L N-methyl pyrrolidone (NMP). This coupling reaction was continued for 1.5 h followed by resin washing with DCM and DMF. Kaiser test was performed to confirm the success of coupling and deprotection steps. The capping was performed using a mixture of NMP, acetic anhydride, and pyridine, followed by resin washing with DCM. All the above steps were repeated until the last monomer was coupled. The PNA was cleaved from the resin using a cleavage cocktail comprising dimethyl sulfide, m-cresol, TMFSA, and TFA (1:1:2:6). The PNA was collected after 1.5 h and precipitated using cold diethyl ether and then centrifuged at 3,500 rpm for 5 min (three times). The PNA was vacuum dried and purified by reverse-phase RP-HPLC (Shimadzu). The PNA concentration was calculated by measuring the absorbance at 260 nm on NanoDrop One (Thermo Fisher Scientific, Waltham, MA) using the extinction coefficient of individual monomers (13,700 M⁻¹ cm⁻¹ [A], 11,700 M⁻¹ cm⁻¹ [G], 8,600 M⁻¹ cm⁻¹ [T], 6,600 M⁻¹ cm⁻¹ [C]). The PNA was freeze dried for conjugating with pHLIP (Labconco, Kansas, MO). pHLIP was purchased commercially from Vivitide peptide (Gardner, MA, USA). The freeze-dried pHLIP was reconstituted in a solution of dimethylsulphoxide:dimethyl formamide in a 1:1 ratio. A solution of 1 mM pHLIP was added to the freeze-dried PNA such that the PNA:pHLIP molar ratio was 1:1.5. The solution was protected from light and agitated on a shaker at 800 rpm for 24 h. The PNA-pHLIP conjugates were purified using RP-HPLC.

Thermal melting: The DNA target was purchased from Keck Oligo. The concentration of PNA and DNA target was measured using NanoDrop. The PNA and DNA were taken in a ratio of 1:1. The samples were made in high-salt buffer (2 mM MgCl₂, 150 mM KCl, 10 mM sodium phosphate). The samples were heated at 95°C for 2 min, and the sample temperature was brought to room temperature. The absorbance of samples was measured using UV visible spectrophotometer wherein the samples were first run from 95°C to 25°C at the rate of 0.2°C min⁻¹ followed by heating back from 25°C to 95°C. Cuvettes of 1-cm path length and 1,000-μL sample volume were used for the experiment.

Gel shift assay: The polyacrylamide gel is prepared by adding 7.3 mL water, 2.5 mL 40% acrylamide/bisacrylamide solution (19:1 ratio), 2.5 mL 5X tris boric EDTA (TBE) buffer, 50 μL 0.5 M EDTA, 125 μL ammonium persulfate (10% w/v), and 12.5 μL TEMED. This solution is mixed and quickly added in between the gel casting plates. A comb is inserted on the top of the gel casting plates to form the wells in the gel. The comb is removed once the gel is solidified, and the gel is placed in the electrophoresis cell, which is then filled with 1X TBE buffer. The samples were made in physiological buffer (2 mM MgCl₂, 150 mM KCl, 10 mM NaPi). The PNA and DNA samples were added in a ratio of 2:1. TCEP was added to the samples in lanes 4, 8, and 12. The samples were incubated for 1 h at 37°C. The samples were subjected to polyacrylamide gel electrophoresis for 120 V for 35 min. The gel was stained with SyBr Gold for 2 min followed by imaging in Gel Doc EZ imager (Bio-Rad).

Simulation system setup and preparation: The amino acid sequence of pHLIP used in this study is AAQNPIYWARYADWL FTTPLLLLDLALLVDADEGTCG. Triggered bilayer

insertion was performed using conventional MD simulations to understand the different conjugated molecules, i.e., pHLIP-PNA, pHLIP-M γ PNA, and pHLIP-S γ PNA. The helical structure of the conjugate molecules was constructed using Avogadro software and the Automated Topology Builder (ATB) platform.^{61–63} The amino acid residues such as Arg on pHLIP were protonated, whereas Glu and Asp were deprotonated, which fits with the experimental condition of pH 6.6 and was confirmed by the calculation from MarvinSketch pKa plugin (<http://www.chemaxon.com/>).^{64,65} Initially, the molecules were given a helical structure with their backbones positioned parallel to the upper leaflet of the bilayer with a COM distance of approximately 2.2 nm using Gromacs 2022 utility gmx editconf.⁶⁶ This initial structure and orientation have been adopted previously for a similar study of various peptide bilayer insertions and membrane perturbations.^{55,67–73} As shown in Figure 2A, a simulation box with dimensions of 6.5 \times 6.5 \times 10 nm³ was initially constructed with the so-called “Berger lipids.”⁷⁴ The lipid bilayer includes 128 POPC molecules with 64 lipids in each monolayer. The initial coordinates were acquired from Dr. Peter Tieleman’s website (<https://people.ucalgary.ca/~tieleman/download.html>). In addition, a total number of 7,864 simple point charge (SPC) water molecules were placed randomly in the simulation box. The concentration of 0.1 M sodium chloride buffer salts, i.e., 26 and 31 Na⁺, was placed randomly in the final solvated system using Gromacs 2022 utility gmx insert-molecule.⁶⁶

Simulation details: The Gromacs 2022 software package with GROMOS96 force fields was used for all MD simulations performed in this study.⁶⁶ The steepest descent algorithm was adopted for the system minimization in 10,000 steps. The first equilibration was implemented under isothermal-isochoric NVT (conserved number of particles N, volume V, and temperature T) for 1 ns at T = 300 K. This was followed by a second equilibration under isothermal-isobaric NPT (conserved number of particles N, pressure P, and temperature T) for another 1 ns at p = 1 bar and T = 300 K. The production runs were carried out for three pHLIP conjugate molecules, i.e., pHLIP-PNA, pHLIP-M γ PNA, and pHLIP-S γ PNA, in the acidic condition of pH 6.6. Each simulation was repeated five times with the new randomly assigned seeds for velocity distribution. The convergence of the potential energy (data not shown here) confirmed the equilibration of the system. Moreover, the production runs were implemented under the NPT ensemble using a Nose-Hoover thermostat and Parrinello-Rahman barostat at p = 1 bar in every 2-fs time step.⁷⁵ The bond lengths of the peptides and lipids were constrained with LINCS. The temperature and pressure coupling were employed with a time constant of 0.1 and 2.0 ps, respectively. Along with particle mesh Ewald (PME) for long-range electrostatics, the periodic boundary conditions (PBCs) were applied for the x, y, and z directions in all simulation systems. The standard cutoff of 1.2 nm was adopted for computing the nonbonded interactions, i.e., Lennard-Jones and electrostatic forces. Trajectory frames such as velocity, forces, and coordinates were saved every 4 ps. The High-Performance Center Supercomputer Cluster (SkyLake Intel; Information Technology Services [ITS], University of Connecticut) was used to run all simulations at approximately 45 ns per day of production.

Cellular uptake by confocal microscopy: U2932 cells were purchased from Leibniz Institute (DSMZ, Germany). To mimic the acidic tumor pH, the pH of L-15 Leibowitz media was lowered to pH 6.4 using 1 N HCl. Around 400,000 U2932 cells were seeded in low pH

media in a 12-well plate, and the cells were immediately treated with 500 nM pHLIP-PNA T5, pHLIP-M γ PNA T6, and pHLIP-S γ PNA T7 and kept in an incubator at 37°C. After 2 h, the cells were harvested and centrifuged at 2,000 rpm at 4°C for 4 min. The cells were then washed with media and resuspended in Hoechst dye and incubated for 20 min in an incubator at 37°C. The cells were washed with media and fixed using 4% formaldehyde for 10 min in an incubator at room temperature. The cells were washed and mounted on a slide using antifade mountant and imaged using Keyence microscope (Itasca, IL, USA).

Cellular uptake by flow cytometry: About 400,000 U2932 cells were seeded in low-pH media in a 12-well plate, and the cells were immediately treated with 500 nM pHLIP-PNA T5, pHLIP-M γ PNA T6, and pHLIP-S γ PNA T7 and kept in an incubator at 37°C. After 4 h, the cells were harvested and centrifuged at 2,000 rpm at 4°C for 4 min. The cells were then washed with media and resuspended in 4% formaldehyde. The cells were analyzed on flow cytometer Fortessa X-20 cell analyzer (BD Biosciences). The data were plotted and analyzed using FlowJo software.

Gene expression: A total of 400,000 cells were seeded in a 12-well plate in low-pH media. The cells were treated with 500 nM pHLIP-Scr-S γ PNA 4, pHLIP-PNA 1, pHLIP-M γ PNA 2, and pHLIP-S γ PNA 3 for 24 h and placed in an incubator at 37°C. The cells were harvested, and the RNA was extracted using the manufacturer's protocol. The RNA concentration was measured using NanoDrop. The cDNA for miR-155 was prepared using 10X RT buffer, reverse transcriptase (50 U/ μ L), RNase inhibitor (20 U/ μ L), deoxyribonucleotide triphosphates (dNTPs; 100 mM), and primers specific for miR-155. Random primers (10X) were used for preparing cDNA for downstream targets. Samples for PCR were prepared using universal master mix and specific TaqMan assays.

Cell viability by MTS assay: A total of 4,000 U2932 cells were seeded in a 96-well plate. The cells were treated with 500 nM pHLIP-Scr-S γ PNA 4, pHLIP-PNA 1, pHLIP-M γ PNA 2, and pHLIP-S γ PNA 3 and placed in an incubator at 37°C. After 24 h, 20 μ L MTS reagent (Promega Corporation) was added to the wells and kept in an incubator for 1 h. The absorbance from the cell plate was measured at 490-nm wavelength using Tecan M Plex plate reader.

Safety assessment by MTS assay: A total of 4,000 HEK293 cells were seeded in a 96-well plate. The cells were treated with 500 nM pHLIP-Scr-S γ PNA 4, pHLIP-PNA 1, pHLIP-M γ PNA 2, and pHLIP-S γ PNA 3 and placed in an incubator at 37°C. Cells treated with PBS were used as a control. After 24 h, 20 μ L MTS reagent (Promega Corporation) was added to the wells and kept in an incubator for 1 h. The absorbance from the cell plate was measured at 490-nm wavelength using Tecan M Plex plate reader.

Annexin V apoptotic assay: A total of 400,000 U2932 cells were seeded in a 12-well plate and treated with 500 nM Scr-S γ PNA 4, pHLIP-PNA 1, pHLIP-M γ PNA 2, and pHLIP-S γ PNA 3 and placed in an incubator at 37°C for 4 h. The cells were harvested and washed with PBS twice by centrifuging the cells at 2,000 rpm for 4 min at 4°C. The cell pellet was resuspended in 1X binding buffer, and the cell count was measured. About 2.3×10^5 cells were transferred to a FACS tube. The cells were stained with 5 μ L PE and 5 μ L

7-amino-actinomycin D (7AAD) dye followed by incubation for 15 min. The volume was made up to 400 μ L with 1X binding buffer, and the cells were analyzed by flow cytometer.

Western blot: A total of 400,000 U2932 cells were seeded in a 12-well plate in low-pH media. The cells were treated with 500 nM Scr-S γ PNA 4, pHLIP-PNA 1, pHLIP-M γ PNA 2, and pHLIP-S γ PNA 3 for 24 h and placed in an incubator at 37°C. The cells were harvested and subjected to protein extraction using 1X RIPA (radioimmunoprecipitation) buffer (Cell Signaling Technologies). The protein was quantified using Lowry assay by reading the absorbance at 750 nm (Tecan M Plex plate reader). The protein samples were made in 4X Laemmli buffer (Bio-Rad) containing 10% mercaptoethanol (Bio-Rad). About 20 μ g protein was loaded on pre-casted gels and run at 200 V for 40 min. The proteins from the gel were transferred to a polyvinylidene fluoride (PVDF) membrane at 110 V for 90 min. The PVDF membrane was blocked in 5% milk for 1 h, followed by washing the blot three times with 1X TBST buffer for 5 min. The antibodies for western blot, Mcl-1 (39224), Vinculin (13901), and anti-rabbit IgG horseradish peroxidase-linked antibody (7074), were purchased from Cell Signaling Technology. The blot was incubated in primary antibody prepared at a dilution of 1:1,000 in 5% bovine serum albumin (BSA; Sigma Aldrich) overnight at 4°C. The next day, the blot was washed three times with 1X TBST buffer for 5 min followed by incubating the blots in secondary antibody prepared in 5% milk at dilution of 1:3,000 for 1 h. The blot was washed three times with 1X TBST buffer for 5 min. The blots were dipped in immobilon chemiluminescent HRP substrate (Millipore) and then imaged using Bio-Rad imager. The intensity from the blots were analyzed by ImageJ software.

Animal studies: All the animal work was performed at the University of Connecticut, Storrs campus, in compliance and approved by the Institutional Animal Care and Use Committee (IACUC). Six-week-old female NSG mice (NOD.Cg-Prkdcscid Il2rgtm1Wjl/SzJ, strain 005557; Jackson Laboratories) were injected with 1×10^7 U2932 cells on the left flank. When the tumors were 100 mm³ in volume, the mice were randomly assigned to a group.

Biodistribution study: When the tumors reached 300 mm³ volume, the mice were injected with a 3 mg kg⁻¹ dose of PBS, pHLIP-PNA T5, pHLIP-M γ PNA T6, and pHLIP-S γ PNA T7 by retro-orbital route. The mice were sacrificed after 24 h, and the organs like liver, lung, tumor, kidney, spleen, and heart were imaged to capture the fluorescent signal in IVIS SpectrumCT imager.

Tissue imaging: The tumor sections were preserved in OCT medium in cryomolds. The tumor was sectioned using cryostat at a thickness of 10 μ m, and the sections were mounted on a glass slide. The slides were washed in PBS two times for 5 min and then dipped in 4% formaldehyde for 10 min. The slides were washed in PBS two times for 5 min after which the slides were dipped in 0.2% Triton X for 20 min. The slides were then washed with PBS two times for 5 min and then were mounted on a slide using antifade mountant with DAPI (Thermo Fisher Scientific, Waltham, MA, USA).

Efficacy study: The mice were randomly divided into PBS, Scr-S γ PNA 4, pHLIP-PNA 1, pHLIP-M γ PNA 2, and pHLIP-S γ PNA 3 treatment groups. The mice were injected with

the respective pHLIP-PNA/ γ PNA or PBS at a dose of 2 mg kg⁻¹ by retro-orbital route. A second dose of 1 mg kg⁻¹ was given after 24 h. The mice were injected with the third dose of 2 mg kg⁻¹ after 24 h. The length, width, and height of tumors were measured daily using vernier caliper. The mice were sacrificed when the tumors reached 2,000 mm³ volume. The mouse organs, such as lung, heart, kidney, spleen, liver, and tumor, were excised. The weights of lung, liver, spleen, and kidney were noted, and the organs were preserved in 10% formalin. The cross-sectional part of the tumor was excised for histology study, and the remaining tumor part was used for RNA and protein extraction. The dissociation medium was prepared using 10% RPMI medium, 1.2 mg mL⁻¹ Dispase, and 0.5 mg mL⁻¹ collagenase. The tumor was minced finely and agitated in the dissociation medium for 1.5h at 37°C. The tumor was centrifuged at 2,000 rpm for 5 min followed by washing with PBS. The cells were incubated in 0.25% trypsin for 3 min followed by adding 10% RPMI medium and passing the cells through a 70- μ m filter. The cells were incubated on 1X RBC lysis buffer on ice for 10 min. This was followed by 1X PBS addition and passing the cells through a 40- μ m filter. The cells were centrifuged and resuspended in 0.5% BSA. The U2932 tumor cells were enriched using the mouse cell depletion kit as per manufacturer's protocol. The enriched cells were used for RNA and protein extraction using the method described above.

IHC staining: The slides were de-waxed in an oven for 15 min and then de-paraffinized in xylene twice for 5 min. The slides were then hydrated using gradient of 100% ethanol, 95% ethanol, and 75% ethanol. The slides were then dipped for 1 h in 1X tris solution pH 6 for antigen retrieval. The slides were then washed with PBST buffer three times for 5 min each. The slides were blocked with 2.5% normal horse serum block for 30 min and then rinsed with PBST for 2 min. The slides were then incubated with primary antibody for 2 h. Ki-67 antibody was used at 1:200 dilution. The slides were rinsed with PBST buffer followed by peroxidase blocking with 3% hydrogen peroxide solution for 10 min. The slides were rinsed in PBST buffer three times for 5 min. The slides were then incubated in chromogen substrate for 5 min. The slides were rinsed in PBST buffer two times for 2 min and then counterstained with hematoxylin for 30 min. The slides were then dehydrated using 95% ethanol for 2 min, 100% ethanol two times for 3 min, and then dipped in xylene twice for 5 min. The slides were air dried and then covered with coverslip. The slides were imaged using Keyence microscope. The Ki-67-positive cells were quantified using ImageJ software.

Supplementary Material

Refer to Web version on PubMed Central for supplementary material.

ACKNOWLEDGMENTS

This work was supported by NIH grants R21CA273042 (to R.B.), 1R21NS114981-01A1 (to R.B.), and R01CA241194 (to R.B. and F.J.S).

REFERENCES

1. Bartel DP (2009). MicroRNAs: target recognition and regulatory functions. *Cell* 136, 215–233. 10.1016/j.cell.2009.01.002. [PubMed: 19167326]

2. Vidigal JA, and Ventura A. (2015). The biological functions of miRNAs: lessons from in vivo studies. *Trends Cell Biol.* 25, 137–147. 10.1016/j.tcb.2014.11.004. [PubMed: 25484347]
3. Van Meter EN, Onyango JA, and Teske KA (2020). A review of currently identified small molecule modulators of microRNA function. *Eur. J. Med. Chem* 188, 112008. 10.1016/j.ejmech.2019.112008. [PubMed: 31931338]
4. Ebert MS, and Sharp PA (2010). MicroRNA sponges: progress and possibilities. *RNA* 16, 2043–2050. 10.1261/rna.2414110. [PubMed: 20855538]
5. Lima JF, Cerqueira L, Figueiredo C, Oliveira C, and Azevedo NF (2018). Anti-miRNA oligonucleotides: A comprehensive guide for design. *RNA Biol.* 15, 338–352. 10.1080/15476286.2018.1445959. [PubMed: 29570036]
6. Stenvang J, Petri A, Lindow M, Obad S, and Kauppinen S. (2012). Inhibition of microRNA function by anti-miR oligonucleotides. *Silence* 3, 1. 10.1186/1758-907x-3-1. [PubMed: 22230293]
7. Gumireddy K, Young DD, Xiong X, Hogenesch JB, Huang Q, and Deiters A. (2008). Small-molecule inhibitors of microRNA miR-21 function. *Angew. Chem., Int. Ed. Engl* 47, 7482–7484. 10.1002/anie.200801555. [PubMed: 18712719]
8. Haniff HS, Liu X, Tong Y, Meyer SM, Knerr L, Lemurell M, Abegg D, Aikawa H, Adibekian A, and Disney MD (2022). A structure-specific small molecule inhibits a miRNA-200 family member precursor and reverses a type 2 diabetes phenotype. *Cell Chem. Biol* 29, 300–311.e10. 10.1016/j.chembiol.2021.07.006.
9. Costales MG, Haga CL, Velagapudi SP, Childs-Disney JL, Phinney DG, and Disney MD (2017). Small Molecule Inhibition of microRNA-210 Reprograms an Oncogenic Hypoxic Circuit. *J. Am. Chem. Soc* 139, 3446–3455. 10.1021/jacs.6b11273. [PubMed: 28240549]
10. Care A, Catalucci D, Felicetti, Bonci D, Addario A, Gallo P, Bang ML, Segnalini P, Gu Y, Dalton ND, et al. (2007). MicroRNA-133 controls cardiac hypertrophy. *Nat. Med* 13, 613–618. 10.1038/nm1582. [PubMed: 17468766]
11. Du C, Liu C, Kang J, Zhao G, Ye Z, Huang S, Li Z, Wu Z, and Pei G. (2009). MicroRNA miR-326 regulates TH-17 differentiation and is associated with the pathogenesis of multiple sclerosis. *Nat. Immunol* 10, 1252–1259. 10.1038/ni.1798. [PubMed: 19838199]
12. Loya CM, Lu CS, Van Vactor D, and Fulga TA (2009). Transgenic microRNA inhibition with spatiotemporal specificity in intact organisms. *Nat. Methods* 6, 897–903. 10.1038/nmeth.1402. [PubMed: 19915559]
13. Krol J, Busskamp V, Markiewicz I, Stadler MB, Ribi S, Richter J, Duebel J, Bicker S, Fehling HJ, Schübeler D, et al. (2010). Characterizing light-regulated retinal microRNAs reveals rapid turnover as a common property of neuronal microRNAs. *Cell* 141, 618–631. 10.1016/j.cell.2010.03.039. [PubMed: 20478254]
14. Krützfeldt J, Rajewsky N, Braich R, Rajeev KG, Tuschl T, Manoharan M, and Stoffel M. (2005). Silencing of microRNAs in vivo with ‘antagomirs’. *Nature* 438, 685–689. 10.1038/nature04303. [PubMed: 16258535]
15. Dhuri K, Bechtold C, Quijano E, Pham H, Gupta A, Vikram A, and Bahal R. (2020). Antisense Oligonucleotides: An Emerging Area in Drug Discovery and Development. *J. Clin. Med* 9, 2004. 10.3390/jcm9062004. [PubMed: 32604776]
16. Esau C, Davis S, Murray SF, Yu XX, Pandey SK, Pear M, Watts L, Booten SL, Graham M, McKay R, et al. (2006). miR-122 regulation of lipid metabolism revealed by in vivo antisense targeting. *Cell Metabol.* 3, 87–98. 10.1016/j.cmet.2006.01.005.
17. Elmén J, Lindow M, Schübeler S, Lawrence M, Petri A, Obad S, Lindholm M, Hedtjärn M, Hansen HF, Berger U, et al. (2008). LNA-mediated microRNA silencing in non-human primates. *Nature* 452, 896–899. 10.1038/nature06783. [PubMed: 18368051]
18. Davis S, Lollo B, Freier S, and Esau C. (2006). Improved targeting of miRNA with antisense oligonucleotides. *Nucleic Acids Res.* 34, 2294–2304. 10.1093/nar/gkl183. [PubMed: 16690972]
19. Gaddam RR, Dhuri K, Kim YR, Jacobs JS, Kumar V, Li Q, Irani K, Bahal R, and Vikram A. (2022). gamma Peptide Nucleic Acid-Based miR-122 Inhibition Rescues Vascular Endothelial Dysfunction in Mice Fed a High-Fat Diet. *J. Med. Chem* 65, 3332–3342. 10.1021/acs.jmedchem.1c01831. [PubMed: 35133835]

20. Nielsen PE, Egholm M, Berg RH, and Buchardt O. (1991). Sequence-selective recognition of DNA by strand displacement with a thymine-substituted polyamide. *Science* 254, 1497–1500. 10.1126/science.1962210. [PubMed: 1962210]
21. Pellestor F, and Paulasova P. (2004). The peptide nucleic acids (PNAs), powerful tools for molecular genetics and cytogenetics. *Eur. J. Hum. Genet* 12, 694–700. 10.1038/sj.ejhg.5201226. [PubMed: 15213706]
22. Dragulescu-Andrasi A, Rapireddy S, Frezza BM, Gayathri C, Gil RR, and Ly DH (2006). A simple gamma-backbone modification preorganizes peptide nucleic acid into a helical structure. *J. Am. Chem. Soc* 128, 10258–10267. 10.1021/ja0625576. [PubMed: 16881656]
23. Sahu B, Sacui I, Rapireddy S, Zanotti KJ, Bahal R, Armitage BA, and Ly DH (2011). Synthesis and characterization of conformationally preorganized, (R)-diethylene glycol-containing gamma-peptide nucleic acids with superior hybridization properties and water solubility. *J. Org. Chem* 76, 5614–5627. 10.1021/jo200482d. [PubMed: 21619025]
24. Crawford T, Moshnikova A, Roles S, Weerakkody D, DuPont M, Carter LM, Shen J, Engelman DM, Lewis JS, Andreev OA, and Reshetnyak YK (2020). pHLIP ICG for delineation of tumors and blood flow during fluorescence-guided surgery. *Sci. Rep* 10, 18356. 10.1038/s41598-020-75443-5. [PubMed: 33110131]
25. Andreev OA, Engelman DM, and Reshetnyak YK (2014). Targeting diseased tissues by pHLIP insertion at low cell surface pH. *Front. Physiol* 5, 97. 10.3389/fphys.2014.00097. [PubMed: 24659971]
26. Reshetnyak YK, Moshnikova A, Andreev OA, and Engelman DM (2020). Targeting Acidic Diseased Tissues by pH-Triggered Membrane-Associated Peptide Folding. *Front. Bioeng. Biotechnol* 8, 335. 10.3389/fbioe.2020.00335. [PubMed: 32411684]
27. Wyatt LC, Moshnikova A, Crawford T, Engelman DM, Andreev OA, and Reshetnyak YK (2018). Peptides of pHLIP family for targeted intracellular and extracellular delivery of cargo molecules to tumors. *Proc. Natl. Acad. Sci. USA* 115, E2811–e2818. 10.1073/pnas.1715350115.
28. Kaplan AR, Pham H, Liu Y, Oyaghire S, Bahal R, Engelman DM, and Glazer PM (2020). Ku80-Targeted pH-Sensitive Peptide-PNA Conjugates Are Tumor Selective and Sensitize Cancer Cells to Ionizing Radiation. *Mol. Cancer Res* 18, 873–882. 10.1158/1541-7786.MCR-19-0661. [PubMed: 32098827]
29. Reshetnyak YK, Andreev OA, Lehnert U, and Engelman DM (2006). Translocation of molecules into cells by pH-dependent insertion of a transmembrane helix. *Proc. Natl. Acad. Sci. USA* 103, 6460–6465. 10.1073/pnas.0601463103. [PubMed: 16608910]
30. Cheng CJ, Bahal R, Babar IA, Pincus Z, Barrera F, Liu C, Svoronos A, Braddock DT, Glazer PM, Engelman DM, et al. (2015). MicroRNA silencing for cancer therapy targeted to the tumour microenvironment. *Nature* 518, 107–110. 10.1038/nature13905. [PubMed: 25409146]
31. Malik S, Lim J, Slack FJ, Braddock DT, and Bahal R. (2020). Next generation miRNA inhibition using short anti-seed PNAs encapsulated in PLGA nanoparticles. *J. Contr. Release* 327, 406–419. 10.1016/j.jconrel.2020.08.026.
32. Ghavami M, Shiraishi T, and Nielsen PE (2020). Enzyme-Triggered Release of the Antisense Octaarginine-PNA Conjugate from Phospholipase A2 Sensitive Liposomes. *ACS Appl. Bio Mater* 3, 1018–1025. 10.1021/acsabm.9b01022.
33. Blanco E, Shen H, and Ferrari M. (2015). Principles of nanoparticle design for overcoming biological barriers to drug delivery. *Nat. Biotechnol* 33, 941–951. 10.1038/nbt.3330. [PubMed: 26348965]
34. Nie S. (2010). Understanding and overcoming major barriers in cancer nanomedicine. *Nanomedicine* 5, 523–528. 10.2217/nnm.10.23. [PubMed: 20528447]
35. Nakamura Y, Mochida A, Choyke PL, and Kobayashi H. (2016). Nanodrug Delivery: Is the Enhanced Permeability and Retention Effect Sufficient for Curing Cancer? *Bioconjugate Chem.* 27, 2225–2238. 10.1021/acs.bioconjchem.6b00437.
36. Kumar V, Wahane A, Gupta A, Manautou JE, and Bahal R. (2023). Multivalent Lactobionic Acid and N-Acetylgalactosamine-Conjugated Peptide Nucleic Acids for Efficient In Vivo Targeting of Hepatocytes. *Adv. Healthcare Mater* 12, e2202859. 10.1002/adhm.202202859.

37. Galbraith WM, Hobson WC, Giclas PC, Schechter PJ, and Agrawal S. (1994). Complement activation and hemodynamic changes following intravenous administration of phosphorothioate oligonucleotides in the monkey. *Antisense Res. Dev* 4, 201–206. 10.1089/ard.1994.4.201. [PubMed: 7849490]
38. Crooke ST, Baker BF, Kwoh TJ, Cheng W, Schulz DJ, Xia S, Salgado N, Bui HH, Hart CE, Burel SA, et al. (2016). Integrated Safety Assessment of 2'-O-Methoxyethyl Chimeric Antisense Oligonucleotides in NonHuman Primates and Healthy Human Volunteers. *Mol. Ther* 24, 1771–1782. 10.1038/mt.2016.136. [PubMed: 27357629]
39. Senn JJ, Burel S, and Henry SP (2005). Non-CpG-containing antisense 2'-methoxyethyl oligonucleotides activate a proinflammatory response independent of Toll-like receptor 9 or myeloid differentiation factor 88. *J. Pharmacol. Exp. Therapeut* 314, 972–979. 10.1124/jpet.105.084004.
40. Henry SP, Seguin R, Cavagnaro J, Berman C, Tepper J, and Kornbrust D. (2016). Considerations for the Characterization and Interpretation of Results Related to Alternative Complement Activation in Monkeys Associated with Oligonucleotide-Based Therapeutics. *Nucleic Acid Therapeut.* 26, 210–215. 10.1089/nat.2015.0593.
41. Bahal R, Quijano E, McNeer NA, Liu Y, Bhunia DC, Lopez-Giraldez F, Fields RJ, Saltzman WM, Ly DH, and Glazer PM (2014). Single-stranded γ PNAs for in vivo site-specific genome editing via Watson-Crick recognition. *Curr. Gene Ther* 14, 331–342. 10.2174/1566523214666140825154158. [PubMed: 25174576]
42. Wang Y, Malik S, Suh HW, Xiao Y, Deng Y, Fan R, Huttner A, Bindra RS, Singh V, Saltzman WM, and Bahal R. (2023). Anti-seed PNAs targeting multiple oncomiRs for brain tumor therapy. *Sci. Adv* 9, eabq7459. 10.1126/sciadv.abq7459.
43. Jurkovicova D, Magyerkova M, Kulcsar L, Krivjanska M, Krivjansky V, Gibadulinova A, Oveckova I, and Chovanec M. (2014). miR-155 as a diagnostic and prognostic marker in hematological and solid malignancies. *Neoplasma* 61, 241–251. 10.4149/neo_2014_032. [PubMed: 24824925]
44. Zheng X, Rui H, Liu Y, and Dong J. (2020). Proliferation and Apoptosis of B-Cell Lymphoma Cells under Targeted Regulation of FOXO3 by miR-155. *Mediterr. J. Hematol. Infect. Dis* 12, e2020073. 10.4084/MJHID.2020.073.
45. Li S, Chen T, Zhong Z, Wang Y, Li Y, and Zhao X. (2012). microRNA-155 silencing inhibits proliferation and migration and induces apoptosis by upregulating BACH1 in renal cancer cells. *Mol. Med. Rep* 5, 949–954. 10.3892/mmr.2012.779. [PubMed: 22307849]
46. Dhuri K, Gaddam RR, Vikram A, Slack FJ, and Bahal R. (2021). Therapeutic Potential of Chemically Modified, Synthetic, Triplex Peptide Nucleic Acid-Based Oncomir Inhibitors for Cancer Therapy. *Cancer Res.* 81, 5613–5624. 10.1158/0008-5472.CAN-21-0736. [PubMed: 34548334]
47. Kim JH, Kim WS, and Park C. (2012). Epstein-Barr virus latent membrane protein-1 protects B-cell lymphoma from rituximab-induced apoptosis through miR-155-mediated Akt activation and up-regulation of Mcl-1. *Leuk. Lymphoma* 53, 1586–1591. 10.3109/10428194.2012.659736. [PubMed: 22268450]
48. Kumar S, Pearse A, Liu Y, and Taylor RE (2020). Modular self-assembly of gamma-modified peptide nucleic acids in organic solvent mixtures. *Nat. Commun* 11, 2960. 10.1038/s41467-020-16759-8. [PubMed: 32528008]
49. Pradeep SP, Malik S, Slack FJ, and Bahal R. (2023). Unlocking the potential of chemically modified peptide nucleic acids for RNA-based therapeutics. *RNA* 29, 434–445. 10.1261/rna.079498.122. [PubMed: 36653113]
50. Dharmaratne NU, Kaplan AR, and Glazer PM (2021). Targeting the Hypoxic and Acidic Tumor Microenvironment with pH-Sensitive Peptides. *Cells* 10. 10.3390/cells10030541.
51. Gayle S, Aiello R, Leelatian N, Beckta JM, Bechtold J, Bourassa P, Csengery J, Maguire RJ, Marshall D, Sundaram RK, et al. (2021). Tumor-selective, antigen-independent delivery of a pH sensitive peptide-topoisomerase inhibitor conjugate suppresses tumor growth without systemic toxicity. *NAR Cancer* 3, zcab021. 10.1093/narcan/zcab021.

52. Bahal R, McNeer NA, Ly DH, Saltzman WM, and Glazer PM (2013). Nanoparticle for delivery of antisense gammaPNA oligomers targeting CCR5. *Artif. DNA PNA XNA* 4, 49–57. 10.4161/adna.25628. [PubMed: 23954968]
53. Wahane A, Malik S, Shih K-C, Gaddam RR, Chen C, Liu Y, Nieh M-P, Vikram A, and Bahal R. (2021). Dual-Modality Poly-l-histidine Nanoparticles to Deliver Peptide Nucleic Acids and Paclitaxel for In Vivo Cancer Therapy. *ACS Appl. Mater. Interfaces* 13, 45244–45258. 10.1021/acscami.1c11981. [PubMed: 34524806]
54. Kasina V, Wahane A, Liu CH, Yang L, Nieh MP, Slack FJ, and Bahal R. (2023). Next-generation poly-L-histidine formulations for miRNA mimic delivery. *Mol. Ther. Methods Clin. Dev* 29, 271–283. 10.1016/j.omtm.2023.03.015. [PubMed: 37123088]
55. Deng Y, Qian Z, Luo Y, Zhang Y, Mu Y, and Wei G. (2013). Membrane binding and insertion of a pHLIP peptide studied by all-atom molecular dynamics simulations. *Int. J. Mol. Sci* 14, 14532–14549. 10.3390/ijms140714532. [PubMed: 23857053]
56. Verona MD, Verdolino V, Palazzesi F, and Corradini R. (2017). Focus on PNA Flexibility and RNA Binding using Molecular Dynamics and Metadynamics. *Sci. Rep* 7, 42799. 10.1038/srep42799. [PubMed: 28211525]
57. Eiriksdóttir E, Konate K, Langel U, Divita G, and Deshayes S. (2010). Secondary structure of cell-penetrating peptides controls membrane interaction and insertion. *Biochim. Biophys. Acta* 1798, 1119–1128. 10.1016/j.bbame.2010.03.005. [PubMed: 20214875]
58. Andreev OA, Karabadzak AG, Weerakkody D, Andreev GO, Engelman DM, and Reshetnyak YK (2010). pH (low) insertion peptide (pHLIP) inserts across a lipid bilayer as a helix and exits by a different path. *Proc. Natl. Acad. Sci. USA* 107, 4081–4086. 10.1073/pnas.0914330107. [PubMed: 20160113]
59. Reshetnyak YK, Segala M, Andreev OA, and Engelman DM (2007). A monomeric membrane peptide that lives in three worlds: in solution, attached to, and inserted across lipid bilayers. *Biophys. J* 93, 2363–2372. 10.1529/biophysj.107.109967. [PubMed: 17557792]
60. Svoronos AA, Bahal R, Pereira MC, Barrera FN, Deacon JC, Bosenberg M, DiMaio D, Glazer PM, and Engelman DM (2020). Tumor-Targeted, Cytoplasmic Delivery of Large, Polar Molecules Using a pH-Low Insertion Peptide. *Mol. Pharm* 17, 461–471. 10.1021/acsmolpharmaceut.9b00883. [PubMed: 31855437]
61. Hanwell MD, Curtis DE, Lonie DC, Vandermeersch T, Zurek E, and Hutchison GR (2012). Avogadro: an advanced semantic chemical editor, visualization, and analysis platform. *J. Cheminf* 4, 17. 10.1186/1758-2946-4-17.
62. Malde AK, Zuo L, Breeze M, Stroet M, Poger D, Nair PC, Oostenbrink C, and Mark AE (2011). An Automated Force Field Topology Builder (ATB) and Repository: Version 1.0. *J. Chem. Theor. Comput* 7, 4026–4037. 10.1021/ct200196m.
63. Koziara KB, Stroet M, Malde AK, and Mark AE (2014). Testing and validation of the Automated Topology Builder (ATB) version 2.0: prediction of hydration free enthalpies. *J. Comput. Aided Mol. Des* 28, 221–233. 10.1007/s10822-014-9713-7. [PubMed: 24477799]
64. Svoronos AA, and Engelman DM (2021). Pharmacokinetic modeling reveals parameters that govern tumor targeting and delivery by a pH-Low Insertion Peptide (pHLIP). *Proc. Natl. Acad. Sci. USA* 118. e2016605118. 10.1073/pnas.2016605118.
65. Duran T, Minatovicz B, Bellucci R, Bai J, and Chaudhuri B. (2022). Molecular Dynamics Modeling Based Investigation of the Effect of Freezing Rate on Lysozyme Stability. *Pharm. Res. (N. Y.)* 39, 2585–2596. 10.1007/s11095-022-03358-z.
66. Van Der Spoel D, Lindahl E, Hess B, Groenhof G, Mark AE, and Berendsen HJC (2005). GROMACS: fast, flexible, and free. *J. Comput. Chem* 26, 1701–1718. 10.1002/jcc.20291. [PubMed: 16211538]
67. Soliman W, Bhattacharjee S, and Kaur K. (2009). Interaction of an antimicrobial peptide with a model lipid bilayer using molecular dynamics simulation. *Langmuir* 25, 6591–6595. 10.1021/la900365g. [PubMed: 19505152]
68. Dunkin CM, Pokorny A, Almeida PF, and Lee HS (2011). Molecular dynamics studies of transportan 10 (tp10) interacting with a POPC lipid bilayer. *J. Phys. Chem. B* 115, 1188–1198. 10.1021/jp107763b. [PubMed: 21194203]

69. Chang Z, Luo Y, Zhang Y, and Wei G. (2011). Interactions of Abeta25–35 beta-barrel-like oligomers with anionic lipid bilayer and resulting membrane leakage: an all-atom molecular dynamics study. *J. Phys. Chem. B* 115, 1165–1174. 10.1021/jp107558e. [PubMed: 21192698]
70. Fleming E, Maharaj NP, Chen JL, Nelson RB, and Elmore DE (2008). Effect of lipid composition on buforin II structure and membrane entry. *Proteins* 73, 480–491. 10.1002/prot.22074. [PubMed: 18452210]
71. Elmore DE (2012). Insights into buforin II membrane translocation from molecular dynamics simulations. *Peptides* 38, 357–362. 10.1016/j.peptides.2012.09.022. [PubMed: 23022591]
72. Zhang Y, Luo Y, Deng Y, Mu Y, and Wei G. (2012). Lipid interaction and membrane perturbation of human islet amyloid polypeptide monomer and dimer by molecular dynamics simulations. *PLoS One* 7, e38191. 10.1371/journal.pone.0038191. [PubMed: 22693597]
73. Duan M, Fan J, and Huo S. (2012). Conformations of islet amyloid polypeptide monomers in a membrane environment: implications for fibril formation. *PLoS One* 7, e47150. 10.1371/journal.pone.0047150.
74. Berger O, Edholm O, and Jähnig F. (1997). Molecular dynamics simulations of a fluid bilayer of dipalmitoylphosphatidylcholine at full hydration, constant pressure, and constant temperature. *Biophys. J* 72, 2002–2013. 10.1016/S0006-3495(97)78845-3. [PubMed: 9129804]
75. Hoover WG (1985). Canonical dynamics: Equilibrium phase-space distributions. *Phys. Rev. A Gen. Phys* 31, 1695–1697. 10.1103/physreva.31.1695. [PubMed: 9895674]

Highlights

Parallel comparison of pHLIP-diethylene glycol γ PNA and pHLIP-serine γ PNA

Computational studies indicated pHLIP-serine γ PNA has optimal transmembrane insertion

pHLIP-serine γ PNA showed higher cellular uptake than other conjugates

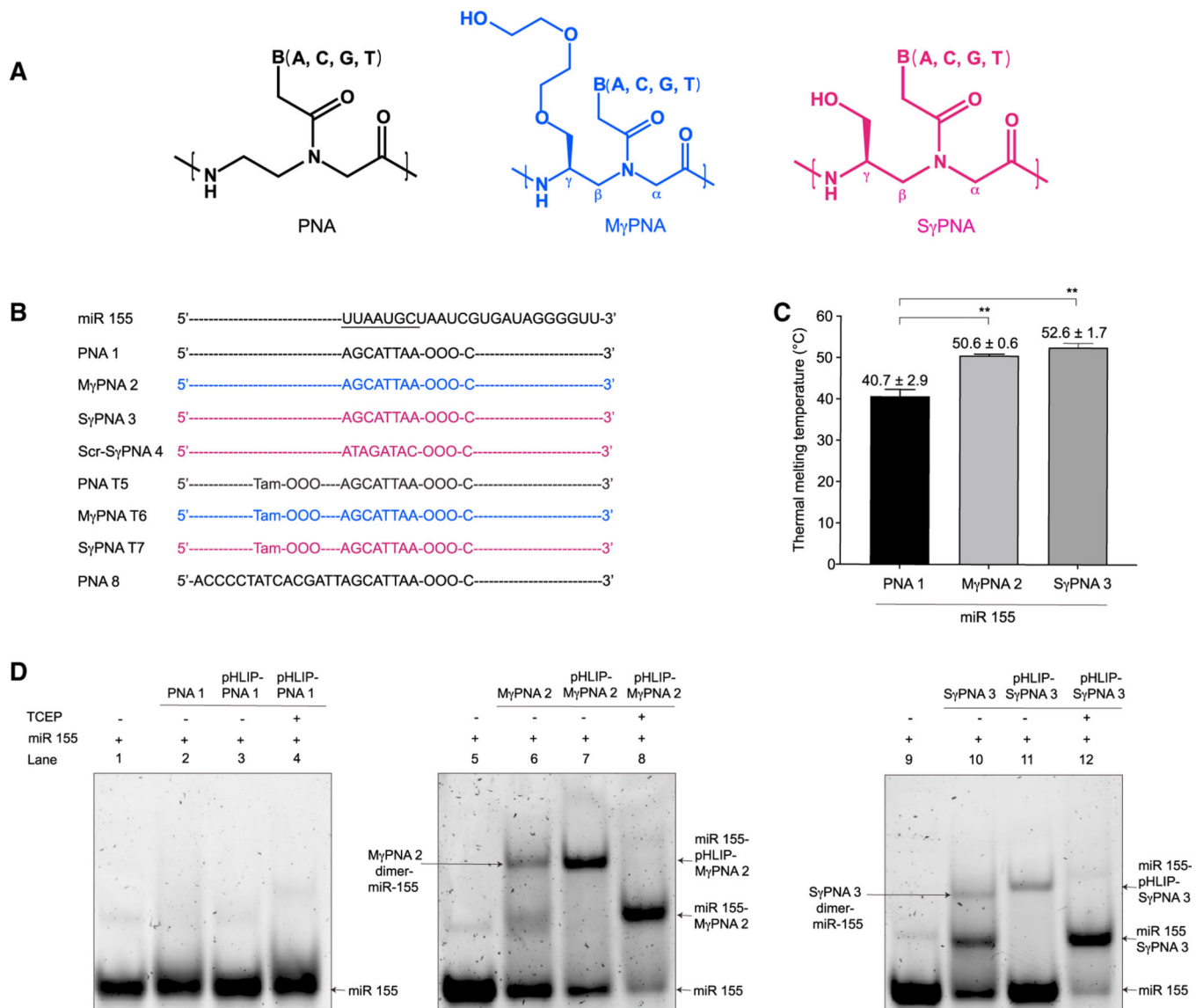


Figure 1. Design of short PNAs and their binding studies

(A) Chemical structures of regular PNA (PNA), miniPEG gamma-modified PNA (M γ PNA), and serine gamma-modified PNA (S γ PNA). B represents nucleobases adenine (A), guanine (G), cytosine (C), and thymine (T).

(B) The sequence of miR-155 with the seed region is underlined. Sequences of short PNAs designed to target the complementary seed region of the miR-155. PNA 1, M γ PNA 2, and S γ PNA 3 sequences are synthesized using regular, miniPEG, and serine monomers. Scr-S γ PNA 4 is the scrambled control. PNA T5, M γ PNA T6, and S γ PNA T7 is conjugated to the fluorescent TAMRA (Tam) dye at 5' terminus. The linker 8-amino-2,6,10-trioxaoctanoic acid is represented as -OOO-. C represents cysteine amino acid. PNA 8 is the full-length regular PNA control.

(C) Thermal melting analysis for PNA 1-miR-155, M γ PNA 2-miR-155, and S γ PNA 3-miR-155 duplex evaluated by UV visible spectrophotometer. The samples were tested in

triplicate ($n = 3$) at a concentration of $4 \mu\text{M}$. Data were plotted as mean and standard error mean (SEM). An unpaired two-tailed t test was used for statistical significance; $**p < 0.01$. (D) Gel shift assay of target miR-155 ($1 \mu\text{M}$) with pHLIP-PNA 1 ($2 \mu\text{M}$), pHLIP-M γ PNA 2 ($2 \mu\text{M}$), and pHLIP-S γ PNA 3 ($2 \mu\text{M}$). Disulfide reduction was performed using 5 mM TCEP. The samples were prepared in high-salt buffer (2 mM MgCl_2 , 150 mM KCl , 10 mM NaPi) and incubated for 1 h at 37°C . The samples were subjected to PAGE separation, and the bands were visualized using SyBr Gold staining.

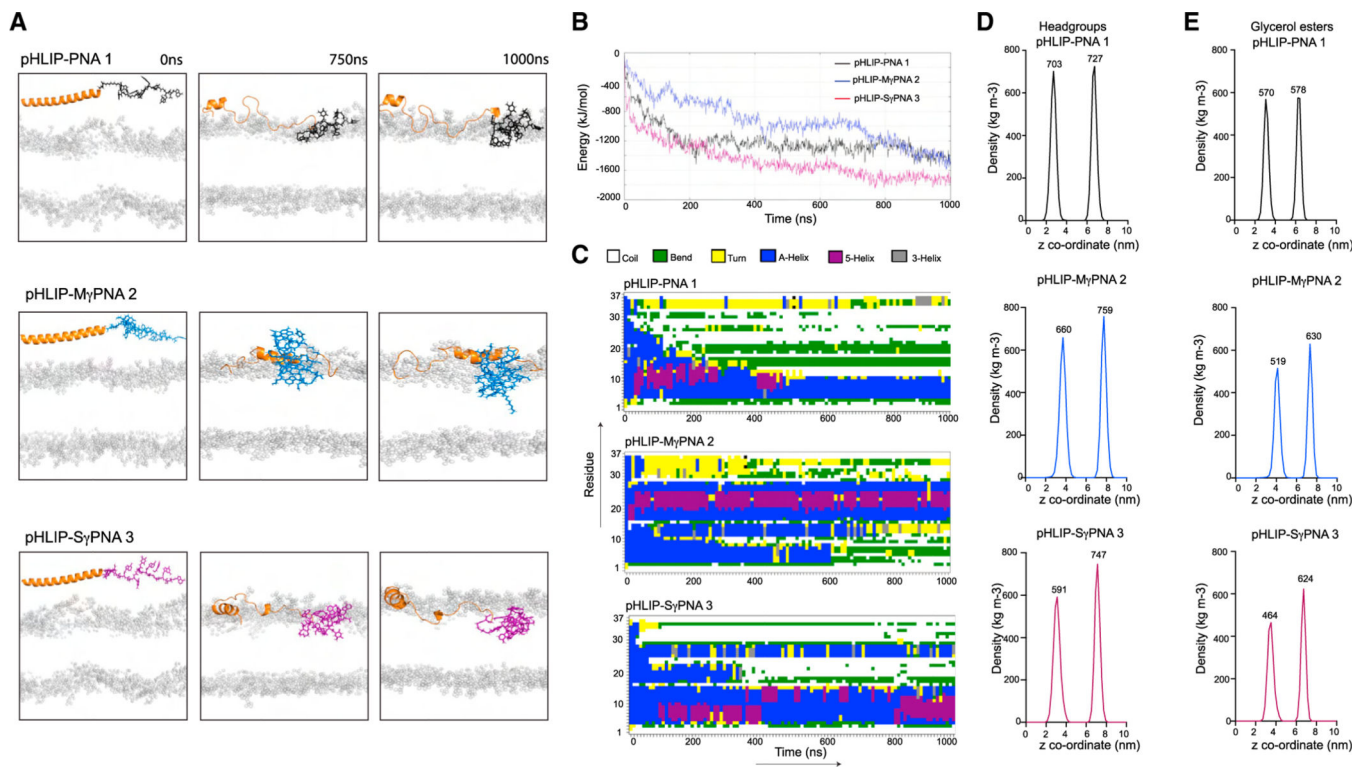


Figure 2. Comparison of pHLIP-PNA and pHLIP- γ PNA interaction with membrane bilayer using molecular dynamics simulation

(A) Snapshots of structures and orientations of pHLIP-PNA 1 (top), pHLIP-M γ PNA 2 (center), and pHLIP-S γ PNA 3 (bottom) at 0, 750, and 1,000 ns. pHLIP is depicted as a ribbon in orange, and PNA 1, M γ PNA 2, and S γ PNA 3 are represented in black, blue, and pink, respectively. The phosphorous atoms of the lipid bilayer are shown as gray spheres.

(B) Profile of total interaction energy (van der Waals energy) between the pHLIP-PNA 1 (black), pHLIP-M γ PNA 2 (blue), and pHLIP-S γ PNA 3 (pink) and membrane bilayer as a function of simulation time.

(C) The define secondary structure of proteins (DSSP) plots for secondary structure transitions as a function of simulation time for pHLIP-PNA 1 (top), pHLIP-M γ PNA 2 (center), and pHLIP-S γ PNA 3 (bottom).

(D) Mass density profiles of phosphate head groups in membrane bilayer for pHLIP-PNA 1 (top, black), pHLIP-M γ PNA 2 (center, blue), and pHLIP-S γ PNA 3 (bottom, pink).

(E) Mass density profiles of glycerol ester groups in membrane bilayer for pHLIP-PNA 1 (top, black), pHLIP-M γ PNA 2 (center, blue), and pHLIP-S γ PNA 3 (bottom, pink).

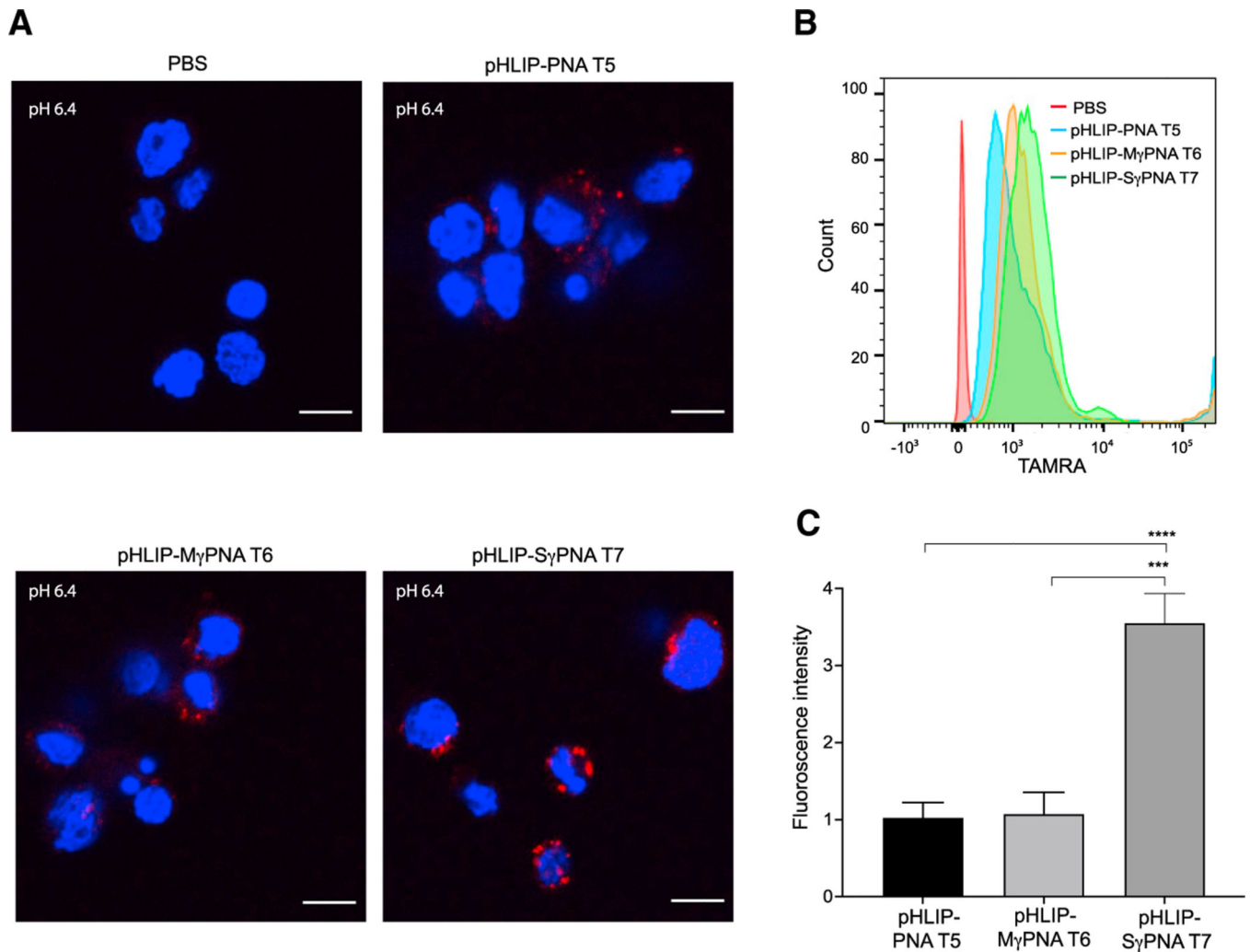


Figure 3. Cellular uptake studies in U2932 cells

(A) Cellular uptake in U2932 cells by confocal microscopy. The experiment was conducted in acidic media conditions (pH 6.4). The cells were treated with a 500 nM pHLIP-PNA-Tamra or pHLIP- γ PNA-Tamra for 4 h. Scale bar, 500 nm. Blue fluorescence represents DAPI, and red fluorescence represents Tamra.

(B) Representative flow cytometry trace of Tamra fluorescence after treatment of U2932 cells with 500 nM dose of pHLIP-PNA T5, pHLIP-M γ PNA T6, and pHLIP-S γ PNA T7 for 4 h.

(C) Quantitative analysis of the fluorescence intensity of pHLIP-PNA-Tamra conjugates in U2932 cells (n = 8); an unpaired t test was used for statistical significance. The data are plotted as mean \pm standard error mean (SEM). ****p < 0.0001; ***p < 0.001.

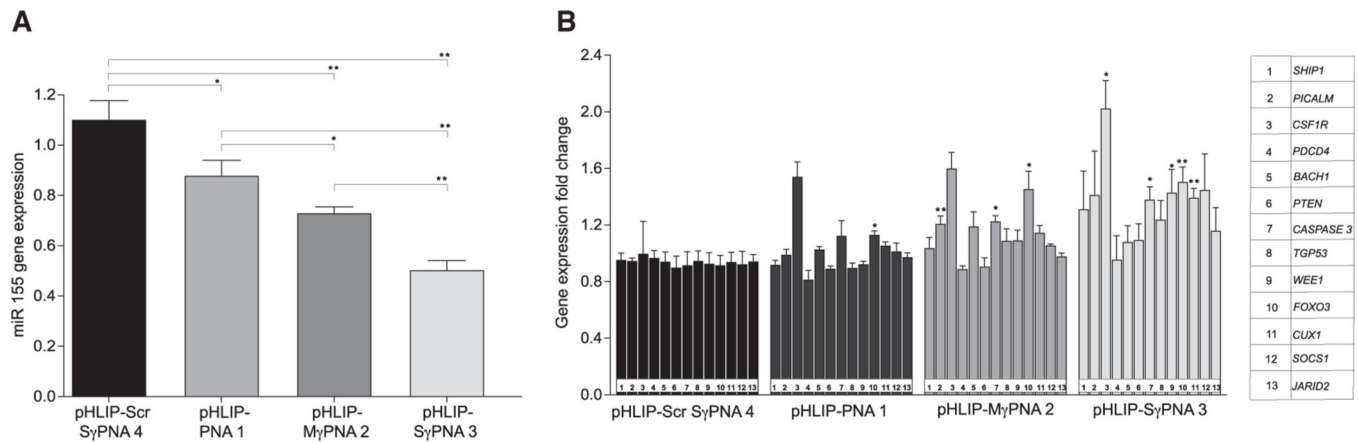


Figure 4. Gene expression analysis in U2932 lymphoma cells

(A) miR-155 gene expression analysis by RT-PCR. U2932 cells were treated with 500 nM dose of pHLIP-PNA or pHLIP- γ PNA for 24 h. The data are normalized to scrambled pHLIP-Scr-S γ PNA 4. Data are represented as mean \pm SEM; n = 9. An unpaired two-tailed t test was used for statistical significance; **p < 0.01; *p < 0.05.

(B) Gene expression levels of downstream targets of miR-155. Data are represented as mean \pm SEM; n = 3. An unpaired two-tailed t test was used for statistical significance; **p < 0.01; *p < 0.05.

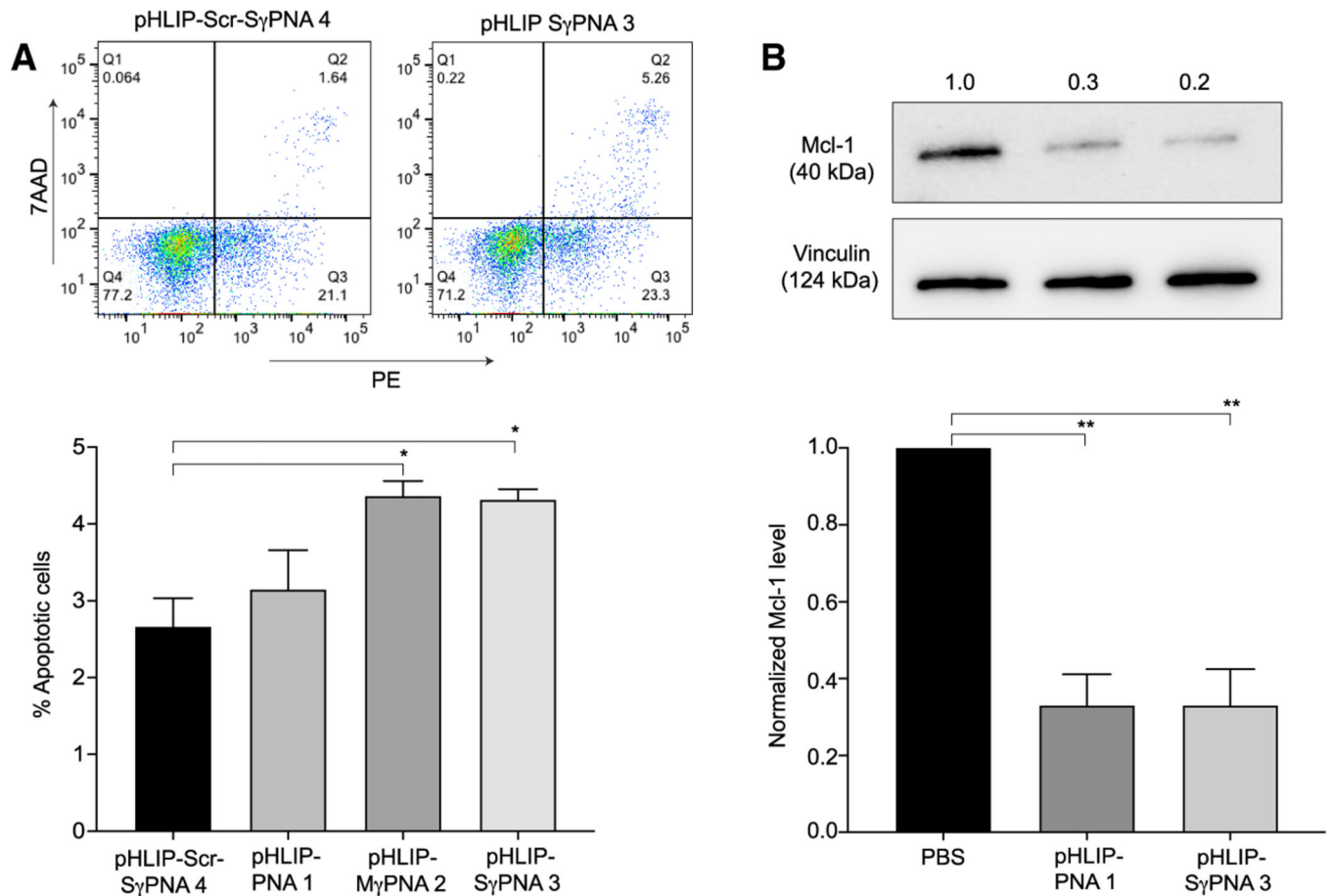


Figure 5. Evaluation of U2932 cell death by multiple functional assays

(A) Quantification of apoptotic cells by Annexin V assay evaluated by flow cytometry. U2932 cells are treated with 500 nM pHLIP-Scr-S γ PNA 4, pHLIP-PNA 1, pHLIP-M γ PNA 2, and pHLIP-S γ PNA 3 for 4 h. Data are plotted as mean \pm SEM (n = 3). Unpaired two-tailed t test was used for statistical significance, *p < 0.05. Representative dot plots of pHLIP-Scr-S γ PNA 4 and pHLIP-S γ PNA 3 are shown.

(B) Representative Mcl-1 western blot and its quantification followed by treatment with the conjugates. The data are plotted as mean \pm SEM. **p < 0.01. The experiments were performed on n = 3 replicates, and an unpaired two-tailed t test was used for statistical significance.

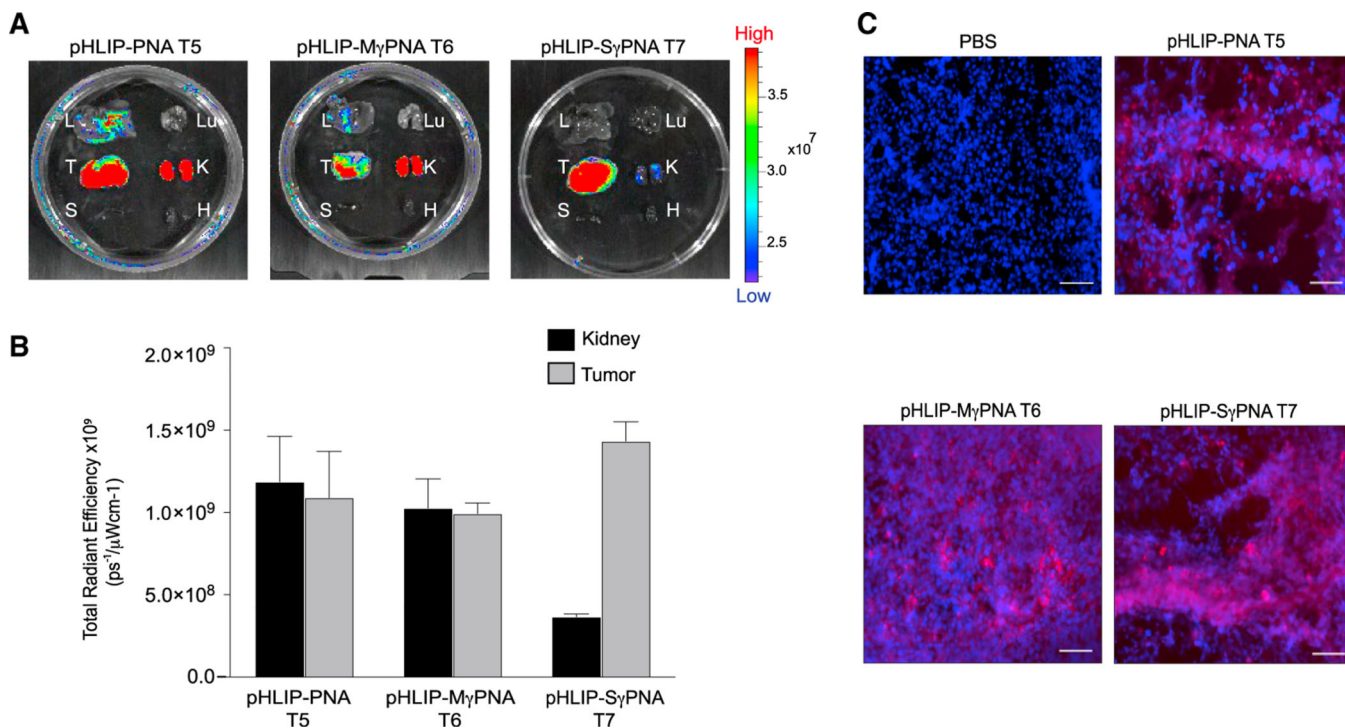


Figure 6. Biodistribution of pHLIP- γ PNA-Tamra conjugates in the U2932-derived xenograft mouse model

(A) IVIS imaging showing biodistribution of pHLIP-PNA T5, pHLIP-M γ PNA T6, and pHLIP-S γ PNA T7 in mouse organs like liver (L), lung (Lu), tumor (T), kidney (K), spleen (S), and heart (H) after 3 mg kg^{-1} dose for 24 h.

(B) Total radiant efficiency calculated from *ex vivo* fluorescence in kidney and tumor after selecting a region of interest (ROI) using IVIS software. Data are represented as mean \pm SEM; $n = 3$.

(C) Biodistribution of pHLIP-PNA T5, pHLIP-M γ PNA T6, and pHLIP-S γ PNA T7 in tumor sections. Blue fluorescence represents DAPI, whereas the red fluorescence represents the respective pHLIP-PNA-tamra or pHLIP- γ PNA-tamra conjugates. Scale bar, 100 μm .

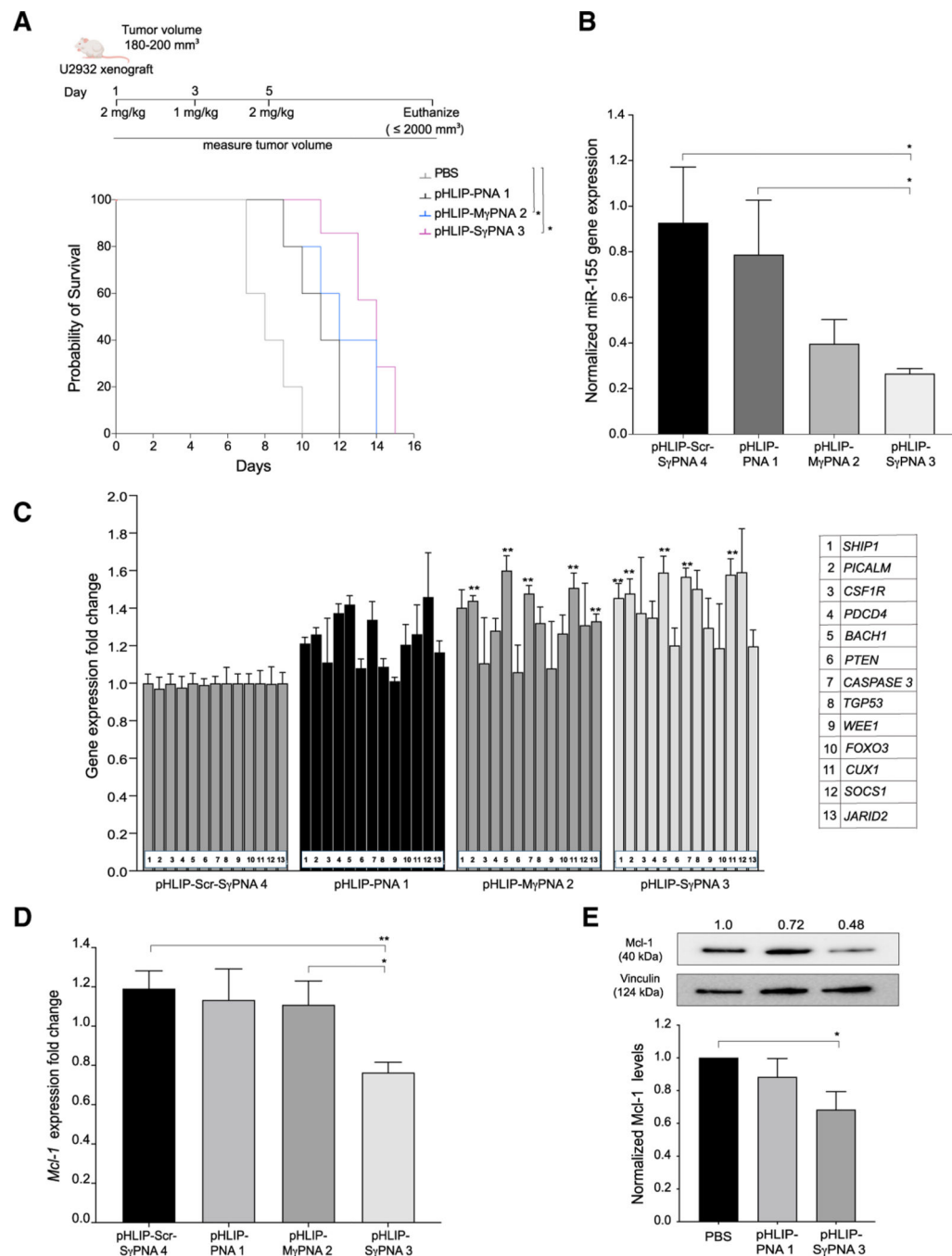


Figure 7. *In vivo* studies in U2932-derived xenograft mouse model

(A) *In vivo* treatment workflow in U2932-derived xenograft mouse model. Survival plot of mice treated with PBS, pHLIP-PNA 1, pHLIP-M γ PNA 2, and pHLIP-S γ PNA 3. Log rank (Mantel-Cox) test was used for statistical analysis; $n = 5$, * $p < 0.05$.

(B) Gene expression levels of miR-155 levels in the tumor samples. The mice treated with pHLIP-Scr-S γ PNA 4 were used as a control. Unpaired two-tailed t test was used for statistical significance. Data are represented as mean \pm SEM; $n = 4$; * $p < 0.05$.

(C) Downstream gene expression levels of tumor suppressor genes. Unpaired two-tailed t test was used for statistical significance; ** $p < 0.01$, * $p < 0.05$. Data are represented as mean \pm SEM; $n = 4$.

(D) Downstream gene expression levels of anti-apoptotic *Mcl-1* gene. Unpaired two-tailed t test was used for statistical significance. Data are represented as mean \pm SEM; $n = 4$; ** $p < 0.01$, * $p < 0.05$.

(E) Mcl-1 protein levels in the tumor samples from mice treated with pHLIP-PNA 1 and pHLIP-S γ PNA 3. The mice supplemented with PBS were used as a control. Unpaired two-tailed t test was used for statistical significance. Data are represented as mean \pm SEM; $n = 3$; * $p < 0.05$.